ELSEVIER

Spectrochimica Acta Part B 56 (2001) 753–776

SPECTROCHIMICA ACTA PART B

www.elsevier.nl/locate/sab

Optical emission spectroscopy and modeling of plasma produced by laser ablation of titanium oxides ☆

A. De Giacomo[a,b,*], V.A. Shakhatov[c], O. De Pascale[c]

[a] *Dipartimento di Chimica, University of Bari, Via Orabona 4, Bari, Italy*
[b] *Centro di studio per la chimica dei plasmi del CNR, Via Orabona 4, Bari, Italy*
[c] *Centro Laser, S.P. per Casamassima, km.3-70010 Valenzano, Bari, Italy*

Received 12 October 2000; accepted 23 April 2001

Abstract

In the present study, the time evolution of electron number density, of electron, atom and ion temperatures, of plasma produced by KrF excimer laser ablation of titanium dioxide and monoxide targets, are investigated by temporally and spatially resolved optical emission spectroscopy over a wide range of laser fluence from 1.7 to 6 J cm^{-2}, oxygen pressures of 10^{-2}–10^{-1} torr and in a vacuum. A state-to-state collisional radiative model is proposed for the first time to interpret the experimental results at a distance of 0.6 mm from the target surface, in vacuum and for a time delay from 100 to 300 ns from the beginning of the laser pulse. In particular, we concentrate our attention on problems concerning the existence of the local thermodynamic conditions in the laser-induced plasma and deviation from them, as observed in our experiment. The numerical model proposed for calculating the electron number density and the population densities of atoms and ions in excited states give good quantitative agreement with the experimental results of the optical emission spectroscopy measurements. © 2001 Elsevier Science B.V. All rights reserved.

Keywords: Laser induced plasma; Local thermodynamic equilibrium; Optical emission spectroscopy; State-to-state collisional radiative model; Titanium oxides

☆ This paper was presented at the 1st International Congress on Laser Induced Plasma Spectroscopy and Applications, Pisa, Italy, October 2000, and is published in the Special Issue of *Spectrochimica Acta Part B*, dedicated to that conference.

* Corresponding author. Tel.: +39-080-4674314; fax: +39-080-4674457.
E-mail address: adg@mail.centrolaser.it (A. De Giacomo).

0584-8547/01/$ - see front matter © 2001 Elsevier Science B.V. All rights reserved.
PII: S0584-8547(01)00224-5

1. Introduction

The flexibility of the experimental set-up and the large quantity of condensed matter material that can be treated by laser, make pulsed laser deposition (PLD) a very promising technique for thin film production [1]. In fact, among conventional techniques [1,2] which are commonly employed for synthesizing titanium dioxide (TiO_2) thin films, the PLD technique has been found to be most satisfactory [3–6]. In particular, plasma assisted pulsed laser deposition has been successfully used for growing TiO_2 thin films [7].

It has been observed that the quality of prepared films is closely related to the deposition conditions such as laser fluence, background oxygen pressure, target-to-substrate distance and substrate temperature [8]. The interaction of laser light with the solid targets is a complicated process and is not yet understood. It consists of different stages: the laser ablation of the target; plasma generation; laser interaction with the plasma; plasma expansion and collision with a substrate. The stages of the plasma generation, laser interaction with plasma and plasma expansion play a very important role in the thin film growth process. In fact, during temporal evolution of the laser-induced plasma (LIP), excitation and ionization of the evaporated material occurs, therefore, it is important to define its thermodynamic parameters, such as electron number density N_e, neutral number density N, temperatures of electrons T_e, atoms T_a and ions T_i. In order to optimize and control the thin film growth process it is necessary to study the dependence of these parameters of the LIP on the deposition conditions and to develop suitable diagnostics.

The traditional set of methods for controlling the parameters of the LIP includes high speed photography, optical emission spectroscopy (OES), mass spectrometry, ion probe detection and time-of-flight detection [1]. Of these, the method of OES is used extensively [9–15]. It is based on the study of the spectral distribution of line intensity and broadening in emission spectra. Electron temperature T_e and number density N_e are determined from relative atomic and ionic line intensity measurements using Boltzmann and Saha–Boltzmann plot techniques [16,17]. The validity of the techniques is based on some assumptions, most importantly those of the existence of local thermodynamic equilibrium (LTE) conditions and optically thin plasma. The fulfillment of LTE conditions in the LIP strongly depend on the experimental conditions such as pressure, duration and intensity of laser radiation, thermophysical properties of the target material and so on [1]. At oxygen pressure low values (10^{-1} torr), which are usually used for pulsed laser deposition of TiO_2 thin films, the parameters of the LIP quickly vary owing to its expansion. Thus, it can lead to a disequilibrium of the forward and backward kinetic processes and so deviations from LTE conditions can occur. In these conditions, electron, ion and atom temperatures can essentially differ. This puts in doubt the initial assumptions about the existence of LTE conditions in the LIP for low pressure applications. The opportunity to detect Stark broadening and displacement of the spectral lines allows electron temperature and number density to be estimated without considering LTE [16,17]. Discrepancy between experimental data obtained by the methods [14] (see also papers cited in [14] for details) does not allow an unequivocal conclusion about the presence of LTE in the LIP to be made. The stage of excitation of the LIP consists of a set of kinetic processes that can have an influence on populations of atoms and ions in electronically excited states. It means that in accordance with the experimental conditions of the PLD, a careful approach is necessary for an estimation of thermodynamic parameters of the LIP by use of spectroscopic measurements.

In spite of the fact that a large number of theoretical works [1,18–23] devoted to research into laser-ablation processes have been carried out, this has not been reflected in the development of the physical models, which would be able to describe and explain observable deviation, in experiments, of the LIP parameters from their values in the LTE conditions. Perhaps the exception is Capitelli et al. [24], where this problem is mentioned and discussed for the first time. According to the authors, one of the important directions to improve our knowledge regarding

this argument is to develop a state-to-state collisional radiative model in order to understand under which experimental condition the deviations of excited state population, from those obtained under LTE conditions, occur.

In this paper we present the results of measurements made by temporal and spatial resolved emission spectroscopy at the time evolution of the electron number density and of the atomic and the ionic state distribution functions (ASDF and ISDF) in the LIP. The ASDF and ISDF occur as a result of the interaction of a KrF excimer laser irradiation with TiO and TiO_2 targets at different values of laser fluence (from 1.7 to 6 J cm^{-2}), of the oxygen pressure at 10^{-2}–10^{-1} torr and in vacuum and distances from the targets up to 6 mm. To interpret the results of measurements of the time evolution of the electron number density N_e, ASDF and ISDF at a distance 0.6 mm from the target surface, in vacuum and for a time delay from 100 to 300 ns from beginning of the laser pulse, a state-to-state collisional radiative model has been developed for the first time. From a comparison of the results of the calculation and experiment we determine the conditions for an expanding high density plasma to be in the LTE as well as the time duration for the existence of such equilibrium.

2. Experimental set-up

The experimental set-up consists of a KrF excimer laser with an optical system in order to steer and focus the laser beam, a PLD vacuum chamber, a system for gas feeding and pumping out, a pressure controlling system and an optical emission spectroscopic system, as depicted in Fig. 1.

The KrF excimer laser with an emission wavelength of 248 nm, as a source of radiation for evaporating the material of the targets, is used in experiments. It is operated in the pulse-periodic regime at a repetition rate, which can change between 1 and 150 Hz. The duration of the output pulses is 30 ns. High voltage on electrodes of the excimer laser discharge cell is automatically readjusted to get constant pulse energy. The laser energy fluctuation is controlled during experiments. Using a beamsplitter, a portion of the laser beam is directed into an energy meter for laser energy detection and monitoring. In this operating mode of the excimer laser, a good reproducibility of the spectroscopic measurement is achieved and laser output energy fluctuations are below 10%. The energy of the laser is varied up to 1.0 J. Using a mirror and lens the laser beam is directed through a quartz window into the PLD chamber and focused onto the target at 45° from the normal surface. The surface of the laser spot is 4×4 mm^2. The energy density of the laser beam is varied up to 6 J cm^{-2}, changing its degree of focusing on the target and the laser energy output.

The targets were fabricated by CERAC from titanium monoxide TiO and titanium dioxide TiO_2 materials (with a purity of 99.99%). During the laser irradiation, the targets are rotated to avoid deep drilling.

The PLD chamber is a typical stainless steel vacuum chamber with a cylindrical build. It is equipped with a rotational holder for the targets, ports for the laser beam, gas pumping out and feeding, pressure gauging and viewports for the OES. The laser material interaction is carried out in vacuum and under oxygen flow.

The chamber is pumped up to 10^{-6} torr by a Blazers rotary and a turbo-molecular pump. Pressure is measured by TPG 300 (total pressure gauge controller blazers). The oxygen flow and pressure (from 10^{-4} to 10^{-1} torr) into chamber are regulated by gas dosing valve.

The emission spectrum from the LIP is detected by two different methods. Time-integrated OES is utilized to identify chemical species generating in the laser-induced plume. Spatially-and-temporally resolved OES is used to investigate the time evolution of a spectral line intensity and broadening, ASDF and ISDF and to estimate electron number density depending on time.

To record a spectral distribution of the line intensity in emission spectra, in a range of wavelengths from 250 up to 700 nm, a high resolution monochromator (HR 640, Instruments S.A., division Jobin Yvon) is applied, equipped with a holographic grating 2400 gr/mm and an intensi-

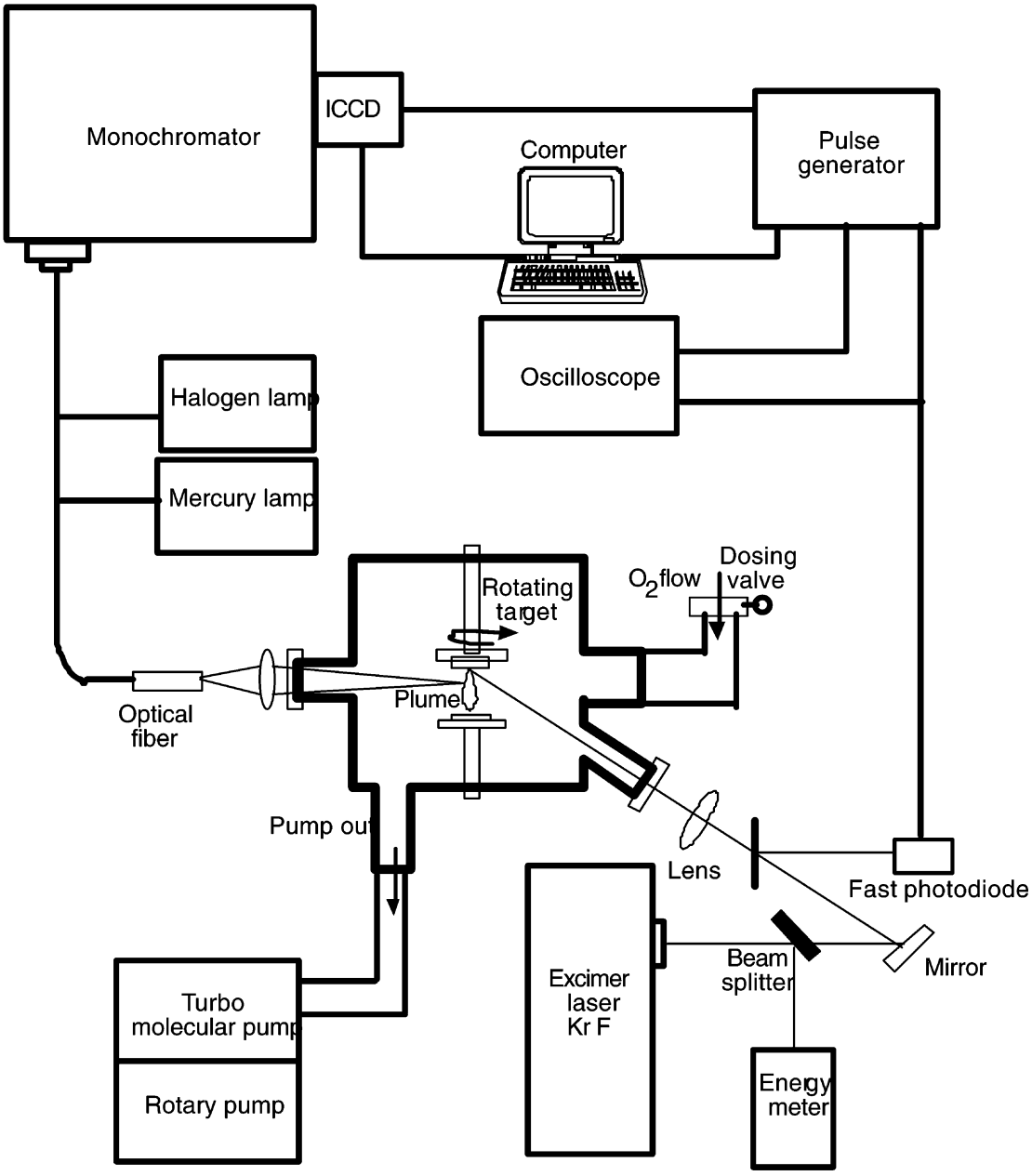

Fig. 1. Schematic diagram of the experimental set-up.

fied charge coupled device (ICCD, ORIEL Instruments) is placed at the exit slit.

The detection of the ICCD output signal is accomplished by a Stanford Research DG 535 programmable pulse generator, connected, through a general purpose interface bus (GPIB), to a personal computer (PC) for data acquisition and processing. To exclude a timing jitter of the excimer laser and spectroscopic systems, a portion of the laser beam by glass wedge is split off

and detected by a fast photodiode in order to trigger the pulsed generator. A digitizing fast oscilloscope (Tektronix TDS 620 A) and a photodiode are used to calibrate and control gate width and time delay after the laser irradiation.

A gate width of 15 ns is used to maximize the spectral line intensity while maintaining good temporal resolution. In a number of experiments, to improve the signal-to-noise ratio the size of the gate width is varied up to 2 μs. Accuracy is achieved by the establishment of the time delay, T_d is 4 ns for a range of T_d changes from 100 to 600 ns. To optimize a signal-to-noise ratio, the monitoring of signals is carried out in an accumulation mode. An average value of the signal from the laser induced plasma is obtained over 150 consecutive laser pulses at a repetition rate of 10 Hz.

The emission spectra are taken from the central part of the LIP at a distance of 0.6, 2, 4 and 6 mm from the target surface with a spatial resolution of 0.5 mm. A quartz lens optically projects the plume image of the LIP, with 1:1 magnification, on the entrance of an optical fiber placed outside of the deposition chamber. So the UV-grade optical fiber (core diameter is 0.5 mm) is placed on the image plane of the plume and is mounted on an optical table, permitting vertical and horizontal micro-movements to collect light emitted from different probe volumes of the LIP. The aperture of the optical fiber is aligned with the centerline of the plume to ensure that the emission signal is collected perpendicularly with respect to its symmetry axes.

The output of the optical fiber is coupled to a slit of the monochromator. This slit width is set at 100 μm. The maximum spectral resolution of the optical system is determined as 0.2 Å, monitoring the lines of a mercury lamp and a He–Ne laser for the slit width was also used in the experiment. The spectral response of the optical system including lens, optical fiber, monochromator and ICCD is controlled with the help of a tungsten halogen lamp. To investigate the spectral shape and width of the investigated lines, the instrumental function of the optical system was measured by a mercury lamp and a He–Ne laser. The line profile is well fitted by a Voigt profile and is characterized by a spectral width 0.9 ± 0.08 Å (FWHM). The ASDF and ISDF are recovered from relative atomic and ionic line intensity measurements [16,17]. For each selected spectral line, a computer code calculates the area from the fit of spectral line shapes with an automatic baseline correction. When line shapes overlap, multiple profile fitting was performed. Such multi-profile fitting is necessary to obtain the correct area from overlapping lines.

3. State-to-state collisional radiative model

The state-to-state collisional radiative model was developed to interpret the results of measurements of the time evolution of electron number density N_e, ASDF and ISDF, recovered from spectroscopic monitoring near the surface of the target at the distance of 0.6 mm, for a gate delay up to 300 ns in vacuum.

In vacuum conditions, during the time when the distance of the plasma front from the target is comparable to the laser spot dimension, the plasma propagation could be considered one-dimensional [25]. In our experiment the spot dimension is approximately 4 mm, thus, the LIP, at the observation point of 0.6 mm from the target, has a uniform distribution for more than 300 ns, if we consider an expansion velocity of 10^5–10^6 cm/s. After these times, the one-dimensional expansion changes into a three-dimensional free expansion and the uniform distribution changes to a non-uniform one, therefore, we applied the model only at this distance.

In the laser-induced evaporation process of TiO and TiO_2 materials ($10^{14} < N$, $N_e < 10^{20}$ cm^{-3}, $10\,000 < T_e$, T_i, $T_a < 30\,000$ K, in vacuum), a number of oxygen and titanium species are generated in the electronically-excited states. The titanium and oxygen atoms and ions are characterized by a considerable number of electronically excited levels as a result of the complexity of their electronic configuration systems. For this reason numerical modeling of kinetic processes taking place in the LIP becomes particularly intricate. We suppose that the predominant kinetic processes that affect the ASDF and ISDF are closely related to colli-

sions of electrons with heavy particles (atoms, ions and molecules) and the kinetic processes in the LIP can be considered independently for each species. Indeed in our test condition, collisions between heavy particles can be ignored for two reasons: first, the LIP is characterized by a high ionization degree [1,24]; second, according to simulation of the proposed model and the experimental data reported in [26–28], the typical values of the rate constants, describing collisions between electron and titanium particles, are greater by two or three orders of magnitude than those between heavy particles (atoms, ions and molecules). Moreover, this conclusion followed immediately from the spectroscopic monitoring of the time evolution of the titanium ionic line intensities, of the titanium ionic and atomic spectral line shapes and of their linewidths. As will be shown, we observed that the spectral line shapes are approximately Lorenzians. Under this condition, the appreciable reduction of ionic line intensities is accompanied by an abrupt diminution of the ionic and atomic spectral linewidths. Therefore, we suppose that the collisions between electrons and heavy particles will be more effective than those between heavy particles. Therefore, we restrict our consideration only to processes involving titanium atoms and ions in the excited states that concern optically allowed transitions. The radiative transitions are arranged within investigated spectral ranges, between 250 and 700 nm, which is of interest from the point of view of LIP monitoring. In order to elucidate the plasma kinetic processes occurring in the LIP, we integrated a system of equations for electron number density, for the populations density of the titanium atoms in sixty-two states and titanium ions in thirty-two states. Tables 1 and 2 list the spectroscopic data for optically allowed transitions from [29,30], which are taken into account in the solution of the system of the kinetic equations. Here, λ is the wavelength in units of nm. The energies of the low state, E_i and E_k, (i) and the upper excited state (k) possess appropriate electronic configurations and terms. The energies are in units of cm^{-1}. The total angular momentums are J_i and J_k. The radiative decay probability, A_{ik}, is in units of 10^8 s^{-1}. The statistical weights are g_i and g_k.

Based on the assumptions mentioned above, we take into account such processes of excitation and de-excitation of titanium atoms and ions as electron impact (inelastic and superelastic collisions). The processes of ionization by electron impact and three-body recombination are the main sources of generation and neutralization of the electrons and ions in the LIP. As this takes place, the dominant process of ionization is an ionization step, at which the atoms, at first, are excited by electronic impacts and the absorption of resonant radiation and then are ionized by the subsequent electron impacts. The processes of photo-ionization of atoms in the excited states and that of radiative recombination can play a significant role in the establishment of the charged particles balance. The processes can proceed especially effective during interaction of the KrF excimer laser ultra violet radiation with the excited atoms. We also take into account the processes of decay of the excited states of atoms and ions by spontaneous and stimulated emission and of their excitation by radiation reabsorption, which can markedly affect the ASDF and ISDF.

Hereby, numerical modeling of the time evolution of the electron number density and the population density is carried out by considering the following collisional–radiative processes [18,24, 31,32], which are responsible for transitions of bound electrons from one excited level (n) to another excited level (m):

Collisional excitation and de-excitation of atoms

$$\mathrm{Ti}(n) + e \Leftrightarrow \mathrm{Ti}(m) + e \tag{1}$$

Collisional excitation and de-excitation of ions

$$\mathrm{Ti}^+(n) + e \Leftrightarrow \mathrm{Ti}^+(m) + e \tag{2}$$

Collisional ionization and three body recombination

$$\mathrm{Ti}(n) + e \Leftrightarrow \mathrm{Ti}^+(m) + e + e \tag{3}$$

Radiative recombination and photo-ionization

$$\mathrm{Ti}^+(n) + e \Leftrightarrow \mathrm{Ti}(m) + h\nu \tag{4}$$

Spontaneous emission, reabsorption and stimulated emission

Table 1
Atomic spectroscopic data

λ (nm)	A_{ki} (10^8 s^{-1})	$E_I - E_k$ (cm^{-1})	Configurations	Terms	$J_i - J_K$	$g_i - g_k$
251.90	5.9×10^{-2}	0.00 – 39686.10	$3d^24s^2 - 3d^3(a\ ^2D)4p$	$^3F - {}^3D°$	2 – 2	5 – 5
252.05	3.8×10^{-1}	0.00 – 39662.15	$3d^24s^2 - 3d^3(a\ ^2D)4p$	$^3F - {}^3D°$	2 – 1	5 – 3
252.80	6.8×10^{-2}	170.13 – 39715.44	$3d^24s^2 - 3d^3(a\ ^2D)4p$	$^3F - {}^3D°$	3 – 3	7 – 7
252.99	3.8×10^{-1}	170.13 – 39686.10	$3d^24s^2 - 3d^3(a\ ^2D)4p$	$^3F - {}^3D°$	3 – 2	7 – 5
254.19	4.3×10^{-1}	386.87 – 39715.44	$3d^24s^2 - 3d^3(a\ ^2D)4p$	$^3F - {}^3D°$	4 – 3	9 – 7
259.02	4.7×10^{-2}	170.13 – 38764.83	$3d^24s^2 - 3d^3(^2P)4p$	$^3F - {}^3D°$	3 – 3	7 – 7
259.36	6.9×10^{-2}	0.00 – 38544.38	$3d^24s^2 - 3d^3(^2G)4p$	$^3F - {}^3F°$	2 – 3	5 – 7
259.66	6.9×10^{-2}	170.13 – 38670.71	$3d^24s^2 - 3d^3(^2G)4p$	$^3F - {}^3F°$	3 – 4	7 – 9
259.99	6.7×10^{-1}	0.00 – 38451.30	$3d^24s^2 - 3d^3(^2G)4p$	$^3F - {}^3F°$	2 – 2	5 – 5
260.51	6.4×10^{-1}	170.13 – 38544.38	$3d^24s^2 - 3d^3(^2G)4p$	$^3F - {}^3F°$	3 – 3	7 – 7
261.13	6.4×10^{-1}	386.87 – 38670.71	$3d^24s^2 - 3d^3(^2G)4p$	$^3F - {}^3F°$	4 – 4	9 – 9
261.15	3.3×10^{-1}	170.13 – 38451.30	$3d^24s^2 - 3d^3(^2G)4p$	$^3F - {}^3F°$	3 – 2	7 – 5
261.99	2.1×10^{-1}	386.87 – 38544.38	$3d^24s^2 - 3d^3(^2G)4p$	$^3F - {}^3F°$	4 – 3	9 – 7
263.15	1.7×10^{-1}	170.13 – 38159.71	$3d^24s^2 - 3d^2(^3P)4s4p(^1P°)$	$^3F - {}^3D°$	3 – 3	7 – 7
263.24	2.7×10^{-1}	0.00 – 37976.78	$3d^24s^2 - 3d^2(^3P)4s4p(^1P°)$	$^3F - {}^3D°$	2 – 2	5 – 5
264.11	1.8	0.00 – 37852.02	$3d^24s^2 - 3d^2(^3P)4s4p(^1P°)$	$^3F - {}^3D°$	2 – 1	5 – 3
264.42	1.4	170.13 – 37976.78	$3d^24s^2 - 3d^2(^3P)4s4p(^1P°)$	$^3F - {}^3D°$	3 – 2	7 – 5
264.66	1.5	386.87 – 38159.71	$3d^24s^2 - 3d^2(^3P)4s4p(^1P°)$	$^3F - {}^3D°$	4 – 3	9 – 7
265.72	8.9×10^{-2}	0.00 – 37555.02	$3d^24s^2 - 3d^3(^2G)4p$	$^3F - {}^3G°$	2 – 3	5 – 7
266.96	1.0×10^{-1}	170.13 – 37617.87	$3d^24s^2 - 3d^3(^2G)4p$	$^3F - {}^3G°$	3 – 4	7 – 9
267.99	1.3×10^{-1}	386.87 – 37690.32	$3d^24s^2 - 3d^3(^2G)4p$	$^3F - {}^3G°$	4 – 5	9 – 11
293.35	9.6×10^{-2}	0.00 – 34078.58	$3d^24s^2 - 3d^2(^1G)4s4p(^3P°)$	$^3F - {}^3F°$	2 – 3	5 – 7
293.73	7.7×10^{-2}	170.13 – 34204.97	$3d^24s^2 - 3d^2(^1G)4s4p(^3P°)$	$^3F - {}^3F°$	3 – 4	7 – 9
294.20	1.0	0.00 – 33980.64	$3d^24s^2 - 3d^2(^1G)4s4p(^3P°)$	$^3F - {}^3F°$	2 – 2	5 – 5
294.83	9.3×10^{-1}	170.13 – 34078.58	$3d^24s^2 - 3d^2(^1G)4s4p(^3P°)$	$^3F - {}^3F°$	3 – 3	7 – 7
295.61	9.7×10^{-1}	386.87 – 34204.97	$3d^24s^2 - 3d^2(^1G)4s4p(^3P°)$	$^3F - {}^3F°$	4 – 4	9 – 9
295.68	1.8×10^{-1}	170.13 – 33980.64	$3d^24s^2 - 3d^2(^1G)4s4p(^3P°)$	$^3F - {}^3F°$	3 – 2	7 – 5
296.72	1.1×10^{-1}	386.87 – 34078.58	$3d^24s^2 - 3d^2(^1G)4s4p(^3P°)$	$^3F - {}^3F°$	4 – 3	9 – 7
297.04	7.4×10^{-2}	0.00 – 33655.85	$3d^24s^2 - 3d^3(^4F)4p$	$^3F - {}^3F°$	2 – 2	5 – 5
298.33	1.1×10^{-1}	170.13 – 33680.13	$3d^24s^2 - 3d^3(^4F)4p$	$^3F - {}^3F°$	3 – 3	7 – 7
300.09	1.2×10^{-1}	386.87 – 33700.87	$3d^24s^2 - 3d^3(^4F)4p$	$^3F - {}^3F°$	4 – 4	9 – 9
318.65	8.0×10^{-1}	0.00 – 31373.80	$3d^24s^2 - 3d^3(^4F)4p$	$^3F - {}^3G°$	2 – 3	5 – 7
319.20	8.5×10^{-1}	170.13 – 31489.45	$3d^24s^2 - 3d^3(^4F)4p$	$^3F - {}^3G°$	3 – 4	7 – 9
319.99	9.4×10^{-1}	386.87 – 31628.67	$3d^24s^2 - 3d^3(^4F)4p$	$^3F - {}^3G°$	4 – 5	9 – 11
320.38	7.2×10^{-2}	170.13 – 31373.80	$3d^24s^2 - 3d^3(^4F)4p$	$^3F - {}^3G°$	3 – 3	7 – 7
321.42	6.5×10^{-2}	386.87 – 31489.45	$3d^24s^2 - 3d^3(^4F)4p$	$^3F - {}^3G°$	4 – 4	9 – 9
334.19	6.5×10^{-1}	0.00 – 29914.72	$3d^24s^2 - 3d^2(^1G)4s4p(^3P°)$	$^3F - {}^3G°$	2 – 3	5 – 7
335.46	6.9×10^{-1}	170.13 – 29971.08	$3d^24s^2 - 3d^2(^1G)4s4p(^3P°)$	$^3F - {}^3G°$	3 – 4	7 – 9
335.83	7.6×10^{-2}	0.00 – 29768.66	$3d^24s^2 - 3d^2(^3F)4s4p(^1P°)$	$^3F - {}^3D°$	2 – 2	5 – 5

Table 1 (*Continued*)

λ (nm)	A_{ki} (10^8 s^{-1})	$E_I - E_k$ (cm^{-1})	Configurations	Terms	$J_i - J_K$	$g_i - g_k$
337.04	7.6×10^{-1}	0.00 – 29661.23	$3d^24s^2 - 3d^2(^3F)4s4p(^1P°)$	$^3F - ^3D°$	2 – 1	5 – 3
337.14	7.2×10^{-1}	386.87 – 30039.21	$3d^24s^2 - 3d^2(^1G)4s4p(^3P°)$	$^3F - ^3G°$	4 – 5	9 – 11
337.76	6.9×10^{-1}	170.13 – 29768.65	$3d^24s^2 - 3d^2(^3F)4s4p(^1P°)$	$^3F - ^3D°$	3 – 2	7 – 5
337.92	6.2×10^{-2}	386.87 – 29971.08	$3d^24s^2 - 3d^2(^1G)4s4p(^3P°)$	$^3F - ^3G°$	4 – 4	9 – 9
338.57	5.2×10^{-2}	386.87 – 29914.72	$3d^24s^2 - 3d^2(^1G)4s4p(^3P°)$	$^3F - ^3G°$	4 – 3	9 – 7
338.59	5.0×10^{-1}	386.87 – 29912.26	$3d^24s^2 - 3d^3(^4F)4p$	$^3F - ^3F$	4 – 3	9 – 7
363.55	8.04×10^{-1}	0.00 – 27498.97	$3d^24s^2 - 3d^2(^3F)4s4p(^1P°)$	$^3F - ^3G°$	2 – 3	5 – 7
363.80	9.3×10^{-3}	0.00 – 27480.05	$3d^24s^2 - 3d^2(^1D)4s4p(^3P°)$	$^3F - ^3D°$	2 – 3	5 – 7
364.27	7.74×10^{-1}	170.13 – 27614.67	$3d^24s^2 - 3d^2(^3F)4s4p(^1P°)$	$^3F - ^3G°$	3 – 4	7 – 9
364.62	2.6×10^{-2}	0.00 – 27418.02	$3d^24s^2 - 3d^2(^1D)4s4p(^3P°)$	$^3F - ^3D°$	2 – 2	5 – 5
365.35	7.54×10^{-1}	386.87 – 27750.12	$3d^24s^2 - 3d^2(^3F)4s4p(^1P°)$	$^3F - ^3G°$	4 – 5	9 – 11
365.46	8.7×10^{-2}	0.00 – 27355.04	$3d^24s^2 - 3d^2(^1D)4s4p(^3P°)$	$^3F - ^3D°$	2 – 1	5 – 3
365.81	5.83×10^{-2}	170.13 – 27498.98	$3d^24s^2 - 3d^2(^3F)4s4p(^1P°)$	$^3F - ^3G°$	3 – 3	7 – 7
366.06	3.0×10^{-2}	170.13 – 27480.05	$3d^24s^2 - 3d^2(^1D)4s4p(^3P°)$	$^3F - ^3D°$	3 – 3	7 – 7
366.90	5.4×10^{-2}	170.13 – 27418.01	$3d^24s^2 - 3d^2(^1D)4s4p(^3P°)$	$^3F - ^3D°$	3 – 2	7 – 5
367.17	4.59×10^{-2}	386.87 – 27614.67	$3d^24s^2 - 3d^2(^3F)4s4p(^1P°)$	$^3F - ^3G°$	4 – 4	9 – 9
368.73	3.5×10^{-3}	386.87 – 27498.98	$3d^24s^2 - 3d^2(^3F)4s4p(^1P°)$	$^3F - ^3G°$	4 – 3	9 – 7
368.99	3.53×10^{-2}	386.87 – 27480.05	$3d^24s^2 - 3d^2(^1D)4s4p(^3P°)$	$^3F - ^3D°$	4 – 3	9 – 7
371.74	4.3×10^{-2}	0.00 – 26892.93	$3d^24s^2 - 3d^2(^1D)4s4p(^3P°)$	$^3F - ^3F°$	2 – 3	5 – 7
372.26	3.4×10^{-2}	170.13 – 27025.65	$3d^24s^2 - 3d^2(^1D)4s4p(^3P°)$	$^3F - ^3F°$	3 – 4	7 – 9
372.98	4.27×10^{-1}	0.00 – 26803.42	$3d^24s^2 - 3d^2(^1D)4s4p(^3P°)$	$^3F - ^3F°$	2 – 2	5 – 5
374.11	4.17×10^{-1}	170.13 – 26892.93	$3d^24s^2 - 3d^2(^1D)4s4p(^3P°)$	$^3F - ^3F°$	3 – 3	7 – 7
375.29	5.04×10^{-1}	386.87 – 27025.65	$3d^24s^2 - 3d^2(^1D)4s4p(^3P°)$	$^3F - ^3F°$	4 – 4	9 – 9
375.36	8.2×10^{-2}	170.13 – 26803.42	$3d^24s^2 - 3d^2(^1D)4s4p(^3P°)$	$^3F - ^3F°$	3 – 2	7 – 5
377.17	6.03×10^{-2}	386.87 – 26892.93	$3d^24s^2 - 3d^2(^1D)4s4p(^3P°)$	$^3F - ^3F°$	4 – 3	9 – 7
389.85	3.48×10^{-3}	0.00 – 25643.70	$3d^24s^2 - 3d^2(^3P)4s4p(^3P°)$	$^3F - ^3F°$	2 – 3	5 – 7
391.47	8.3×10^{-3}	0.00 – 25537.28	$3d^24s^2 - 3d^2(^1D)4s4p(^3P°)$	$^3F - ^3P°$	2 – 1	5 – 3
392.14	2.15×10^{-2}	0.00 – 25493.72	$3d^24s^2 - 3d^2(^1D)4s4p(^3P°)$	$^3F - ^3P°$	2 – 2	5 – 5
392.45	7.15×10^{-2}	170.13 – 25643.70	$3d^24s^2 - 3d^2(^3P)4s4p(^3P°)$	$^3F - ^3F°$	3 – 3	7 – 7
392.99	7.52×10^{-2}	0.00 – 25438.90	$3d^24s^2 - 3d^2(^1D)4s4p(^3P°)$	$^3F - ^3F°$	2 – 2	5 – 5
394.78	9.6×10^{-2}	170.13 – 25493.72	$3d^24s^2 - 3d^2(^1D)4s4p(^3P°)$	$^3F - ^3P°$	3 – 2	7 – 5
394.87	4.85×10^{-1}	0.00 – 25317.81	$3d^24s^2 - 3d^3(^4F)4p$	$^3F - ^3D°$	2 – 1	5 – 3
395.63	3.00×10^{-1}	170.13 – 25438.90	$3d^24s^2 - 3d^2(^1D)4s4p(^3P°)$	$^3F - ^3F°$	3 – 2	7 – 5
395.82	4.05×10^{-1}	386.87 – 25643.70	$3d^24s^2 - 3d^2(^3P)4s4p(^3P°)$	$^3F - ^3F°$	4 – 3	9 – 7
396.29	4.13×10^{-2}	0.00 – 25227.22	$3d^24s^2 - 3d^2(^3F)4s4p(^1P°)$	$^3F - ^3F°$	2 – 3	5 – 7
396.43	3.09×10^{-2}	170.13 – 25388.33	$3d^24s^2 - 3d^2(^3F)4s4p(^1P°)$	$^3F - ^3F°$	3 – 4	7 – 9
398.18	3.76×10^{-1}	0.00 – 25107.42	$3d^24s^2 - 3d^2(^3F)4s4p(^1P°)$	$^3F - ^3F°$	2 – 2	5 – 5
398.98	3.79×10^{-1}	170.13 – 25227.22	$3d^24s^2 - 3d^2(^3F)4s4p(^1P°)$	$^3F - ^3F°$	3 – 3	7 – 7
399.86	4.08×10^{-1}	386.87 – 25388.33	$3d^24s^2 - 3d^2(^3F)4s4p(^1P°)$	$^3F - ^3F°$	4 – 4	9 – 9
400.89	7.03×10^{-2}	170.13 – 25107.42	$3d^24s^2 - 3d^2(^3F)4s4p(^1P°)$	$^3F - ^3F°$	3 – 2	7 – 5
402.46	6.14×10^{-2}	386.87 – 25227.22	$3d^24s^2 - 3d^2(^3F)4s4p(^1P°)$	$^3F - ^3F°$	4 – 3	9 – 7
458.81	8.4×10^{-2}	20126.06 – 42107.06	$3d^2(^3F)4s4p(^3P°) - 3d^24s(^4F)4d$	$^3D° - ^3F$	3 – 4	7 – 9

Table 1 (*Continued*)

λ (nm)	A_{ki} (10^8 s^{-1})	$E_I - E_k$ (cm^{-1})	Configurations	Terms	$J_i - J_K$	$g_i - g_k$
465.65	1.99×10^{-2}	0.00 − 21469.49	$3d^24s^2 - 3d^2(^3F)4s4p(^3P°)$	$^3F - ^3G°$	2 − 3	5 − 7
466.76	2.18×10^{-2}	170.13 − 21588.50	$3d^24s^2 - 3d^2(^3F)4s4p(^3P°)$	$^3F - ^3G°$	3 − 4	7 − 9
468.19	2.35×10^{-2}	386.87 − 21739.71	$3d^24s^2 - 3d^2(^3F)4s4p(^3P°)$	$^3F - ^3G°$	4 − 5	9 − 11
469.37	8.5×10^{-4}	170.13 − 21469.49	$3d^24s^2 - 3d^2(^3F)4s4p(^3P°)$	$^3F - ^3G°$	3 − 3	7 − 7
471.53	6.9×10^{-4}	386.87 − 21588.50	$3d^24s^2 - 3d^2(^3F)4s4p(^3P°)$	$^3F - ^3G°$	4 − 4	9 − 9
499.70	4.07×10^{-3}	0.00 − 20006.03	$3d^24s^2 - 3d^2(^3F)4s4p(^3P°)$	$^3F - ^3D°$	2 − 2	5 − 5
500.96	2.09×10^{-3}	170.13 − 20126.06	$3d^24s^2 - 3d^2(^3F)4s4p(^3P°)$	$^3F - ^3D°$	3 − 3	7 − 7
501.42	5.3×10^{-2}	0.00 − 19937.86	$3d^24s^2 - 3d^2(^3F)4s4p(^3P°)$	$^3F - ^3D°$	2 − 1	5 − 3
504.00	3.89×10^{-2}	170.13 − 20006.03	$3d^24s^2 - 3d^2(^3F)4s4p(^3P°)$	$^3F - ^3D°$	3 − 2	7 − 5
506.41	1.3×10^{-1}	21739.71 − 41481.13	$3d^2(^3F)4s4p(^3P°) - 3d^24s(^3F)4d$	$^3G° - ^3G$	5 − 5	11 − 11
506.47	3.79×10^{-2}	386.87 − 20126.06	$3d^24s^2 - 3d^2(^3F)4s4p(^3P°)$	$^3F - ^3D°$	4 − 3	9 − 7
514.75	3.50×10^{-3}	0.00 − 19421.60	$3d^24s^2 - 3d^2(^3F)4s4p(^3P°)$	$^3F - ^3F°$	2 − 3	5 − 7
515.22	2.64×10^{-3}	170.13 − 19573.97	$3d^24s^2 - 3d^2(^3F)4s4p(^3P°)$	$^3F - ^3F°$	3 − 4	7 − 9
517.37	3.80×10^{-2}	0.00 − 19322.99	$3d^24s^2 - 3d^2(^3F)4s4p(^3P°)$	$^3F - ^3F°$	2 − 2	5 − 5
519.30	3.49×10^{-2}	170.13 − 19421.58	$3d^24s^2 - 3d^2(^3F)4s4p(^3P°)$	$^3F - ^3F°$	3 − 3	7 − 7
521.04	3.57×10^{-2}	386.87 − 19573.97	$3d^24s^2 - 3d^2(^3F)4s4p(^3P°)$	$^3F - ^3F°$	4 − 4	9 − 9
521.97	2.50×10^{-3}	170.13 − 19322.99	$3d^24s^2 - 3d^2(^3F)4s4p(^3P°)$	$^3F - ^3F°$	3 − 2	7 − 5
525.20	1.23×10^{-1}	386.87 − 19421.58	$3d^24s^2 - 3d^2(^3F)4s4p(^3P°)$	$^3F - ^3F°$	4 − 3	9 − 7
564.86	1.3×10^{-1}	20126.06 − 37824.75	$3d^2(^3F)4s4p(^3P°) - 3d^24s(^4F)5s$	$^3D° - ^3F$	3 − 4	7 − 9
567.99	1.1×10^{-1}	19937.86 − 37538.80	$3d^2(^3F)4s4p(^3P°) - 3d^24s(^4F)5s$	$^3D° - ^3F$	1 − 2	3 − 5
622.05	1.8×10^{-1}	21588.50 − 37659.93	$3d^2(^3F)4s4p(^3P°) - 3d^24s(^4F)5s$	$^3D° - ^3F$	4 − 3	9 − 7

Table 2
Ionic spectroscopic data

λ (nm)	A_{ki} (10^8 s^{-1})	$E_i - E_k$ (cm^{-1})	Configurations	Terms	$J_i - J_K$	$g_i - g_k$
251.09	2.8×10^{-3}	938.89 – 40798.30	$3d^3 - 3d^2(^3P)4p$	$^4F - ^4D°$	5/2 – 7/2	6 – 8
251.98	4.9×10^{-3}	908.02 – 40581.49	$3d^3 - 3d^2(^3P)4p$	$^4F - ^4D°$	3/2 – 5/2	4 – 6
252.46	1.2×10^{-1}	983.89 – 40581.49	$3d^3 - 3d^2(^3P)4p$	$^4F - ^4D°$	5/2 – 5/2	6 – 6
252.98	1.7×10^{-1}	908.02 – 40425.59	$3d^3 - 3d^2(^3P)4p$	$^4F - ^4D°$	3/2 – 3/2	4 – 4
253.46	5.4×10^{-1}	983.89 – 40425.59	$3d^3 - 3d^2(^3P)4p$	$^4F - ^4D°$	5/2 – 3/2	6 – 4
253.59	6.8×10^{-1}	908.02 – 40330.16	$3d^3 - 3d^2(^3P)4p$	$^4F - ^4D°$	3/2 – 1/2	4 – 2
263.55	1.9	30836.32 – 68769.19	$3d^2(^3F)4p - 3d^2(^3F)4d$	$^4F° - ^4F$	3/2 – 3/2	4 – 4
263.86	1.7	30958.50 – 68846.52	$3d^2(^3F)4p - 3d^2(^3F)4d$	$^4F° - ^4F$	5/2 – 5/2	6 – 6
264.20	1.9	31113.65 – 68951.98	$3d^2(^3F)4p - 3d^2(^3F)4d$	$^4F° - ^4F$	7/2 – 7/2	8 – 8
264.59	2.7	31301.01 – 69084.44	$3d^2(^3F)4p - 3d^2(^3F)4d$	$^4F° - ^4F$	9/2 – 9/2	10 – 10
275.27	1.1	32767.07 – 69084.44	$3d^2(^3F)4p - 3d^2(^3F)4d$	$^4D° - ^4F$	7/2 – 9/2	8 – 10
275.75	7.2×10^{-1}	32697.99 – 68951.98	$3d^2(^3F)4p - 3d^2(^3F)4d$	$^4D° - ^4F$	5/2 – 7/2	6 – 8
275.83	9.9×10^{-1}	32602.55 – 68846.52	$3d^2(^3F)4p - 3d^2(^3F)4d$	$^4D° - ^4F$	3/2 – 5/2	4 – 6
275.88	4.4×10^{-1}	32532.21 – 68769.19	$3d^2(^3F)4p - 3d^2(^3F)4d$	$^4D° - ^4F$	1/2 – 3/2	2 – 4
276.28	7.2×10^{-2}	32767.07 – 68951.98	$3d^2(^3F)4p - 3d^2(^3F)4d$	$^4D° - ^4F$	7/2 – 7/2	8 – 8
276.42	7.4×10^{-1}	32602.55 – 68769.19	$3d^2(^3F)4p - 3d^2(^3F)4d$	$^4D° - ^4F$	3/2 – 3/2	4 – 4
280.48	4.6	29544.37 – 65186.75	$3d^2(^3F)4p - 3d^2(^3F)4d$	$^4G° - ^4H$	5/2 – 7/2	6 – 8
281.02	5.1	29734.54 – 65308.30	$3d^2(^3F)4p - 3d^2(^3F)4d$	$^4G° - ^4H$	7/2 – 9/2	8 – 10
281.78	3.8	29968.30 – 65446.27	$3d^2(^3F)4p - 3d^2(^3F)4d$	$^4G° - ^4H$	9/2 – 11-2	10 – 12
281.99	6.5×10^{-1}	29734.54 – 65186.75	$3d^2(^3F)4p - 3d^2(^3F)4d$	$^4G° - ^4H$	7/2 – 7/2	8 – 8
282.13	7.9×10^{-1}	29544.37 – 64979.15	$3d^2(^3F)4p - 3d^2(^3F)4d$	$^4G° - ^4G$	5/2 – 7/2	6 – 8
282.87	1.2	29544.37 – 64886.48	$3d^2(^3F)4p - 3d^2(^3F)4d$	$^4G° - ^4G$	5/2 – 5/2	6 – 6
282.88	9.1×10^{-1}	29968.30 – 65308.30	$3d^2(^3F)4p - 3d^2(^3F)4d$	$^4G° - ^4H$	9/2 – 9/2	10 – 10
283.40	7.9×10^{-1}	29968.30 – 65243.46	$3d^2(^3F)4p - 3d^2(^3F)4d$	$^4G° - ^4G$	9/2 – 11/2	10 – 12
283.65	1.2	29734.54 – 64979.15	$3d^2(^3F)4p - 3d^2(^3F)4d$	$^4G° - ^4G$	7/2 – 7/2	8 – 8
284.40	1.5×10^{-1}	29734.54 – 64886.48	$3d^2(^3F)4p - 3d^2(^3F)4d$	$^4G° - ^4G$	7/2 – 5/2	8 – 6
284.59	1.2	29968.30 – 65095.80	$3d^2(^3F)4p - 3d^2(^3F)4d$	$^4G° - ^4G$	9/2 – 9/2	10 – 10
285.54	1.4×10^{-1}	29968.30 – 64979.15	$3d^2(^3F)4p - 3d^2(^3F)4d$	$^4G° - ^4G$	9/2 – 7/2	10 – 8
290.99	7.9×10^{-3}	393.44 – 34748.40	$3d^2(^3F)4s - 3d^2(^3F)4p$	$^4F - ^4G°$	9/2 – 9/2	10 – 10
293.60	2.7	30836.32 – 64886.48	$3d^2(^3F)4p - 3d^2(^3F)4d$	$^4F° - ^4G$	3/2 – 5/2	4 – 6
293.85	2.4	30958.50 – 64979.15	$3d^2(^3F)4p - 3d^2(^3F)4d$	$^4F° - ^4G$	5/2 – 7/2	6 – 8
294.19	1.8	31113.65 – 65095.80	$3d^2(^3F)4p - 3d^2(^3F)4d$	$^4F° - ^4G$	7/2 – 9/2	8 – 10
294.53	2.7	31301.01 – 65243.46	$3d^2(^3F)4p - 3d^2(^3F)4d$	$^4F° - ^4G$	9/2 – 11/2	10 – 12
295.20	3.0×10^{-1}	31113.65 – 64979.15	$3d^2(^3F)4p - 3d^2(^3F)4d$	$^4F° - ^4G$	7/2 – 7/2	8 – 8
295.82	1.4×10^{-1}	31301.01 – 65095.80	$3d^2(^3F)4p - 3d^2(^3F)4d$	$^4F° - ^4G$	9/2 – 9/2	10 – 10
305.74	2.2×10^{-2}	0.00 – 32697.99	$3d^2(^3F)4s - 3d^2(^3F)4p$	$^4F - ^4D°$	3/2 – 5/2	4 – 6
306.62	2.53×10^{-1}	94.10 – 32697.99	$3d^2(^3F)4s - 3d^2(^3F)4p$	$^4F - ^4D°$	5/2 – 5/2	6 – 6
306.64	3.3×10^{-1}	0.00 – 32602.55	$3d^2(^3F)4s - 3d^2(^3F)4p$	$^4F - ^4D°$	3/2 – 3/2	4 – 4
307.21	2.0×10^{-1}	225.73 – 32767.07	$3d^2(^3F)4s - 3d^2(^3F)4p$	$^4F - ^4D°$	7/2 – 7/2	8 – 8

Table 2 (*Continued*)

λ (nm)	A_{ki} (10^8 s^{-1})	$E_i - E_k$ (cm^{-1})	Configurations	Terms	$J_i - J_K$	$g_i - g_k$
251.09	2.8×10^{-3}	938.89 – 40798.30	$3d^3 - 3d^2(^3P)4p$	$^4F - ^4D°$	5/2 – 7/2	6 – 8
307.30	1.6	0.00 – 32532.21	$3d^2(^3F)4s - 3d^2(^3F)4p$	$^4F - ^4D°$	3/2 – 7/2	4 – 2
307.52	1.13	94.10 – 32602.55	$3d^2(^3F)4s - 3d^2(^3F)4p$	$^4F - ^4D°$	5/2 – 3/2	6 – 4
307.87	1.09	225.73 – 32697.99	$3d^2(^3F)4s - 3d^2(^3F)4p$	$^4F - ^4D°$	7/2 – 5/2	8 – 6
308.80	1.25	393.44 – 32767.07	$3d^2(^3F)4s - 3d^2(^3F)4p$	$^4F - ^4D°$	9/2 – 7/2	10 – 8
314.47	4.2×10^{-3}	908.02 – 32697.99	$3d^3 - 3d^2(^3F)4p$	$^4F - ^4D°$	3/2 – 5/2	4 – 6
314.54	1.7×10^{-3}	983.89 – 32767.07	$3d^3 - 3d^2(^3F)4p$	$^4F - ^4D°$	5/2 – 7/2	6 – 8
315.23	9.4×10^{-2}	983.89 – 32697.99	$3d^3 - 3d^2(^3F)4p$	$^4F - ^4D°$	5/2 – 5/2	6 – 6
315.42	1.1×10^{-1}	908.02 – 32602.55	$3d^3 - 3d^2(^3F)4p$	$^4F - ^4D°$	3/2 – 3/2	4 – 4
316.12	5.9×10^{1}	908.02 – 32532.21	$3d^3 - 3d^2(^3F)4p$	$^4F - ^4D°$	3/2 – 1/2	4 – 2
316.18	4.6×10^{1}	983.89 – 32602.55	$3d^3 - 3d^2(^3F)4p$	$^4F - ^4D°$	5/2 – 3/2	6 – 4
321.71	1.69×10^{-1}	225.73 – 31301.01	$3d^2(^3F)4s - 3d^2(^3F)4p$	$^4F - ^4F°$	7/2 – 9/2	8 – 10
322.28	2.6×10^{-1}	94.10 – 31113.65	$3d^2(^3F)4s - 3d^2(^3F)4p$	$^4F - ^4F°$	5/2 – 7/2	6 – 8
323.45	1.38	393.44 – 31301.01	$3d^2(^3F)4s - 3d^2(^3F)4p$	$^4F - ^4F°$	9/2 – 9/2	10 – 10
323.66	1.11	225.73 – 31113.65	$3d^2(^3F)4s - 3d^2(^3F)4p$	$^4F - ^4F°$	7/2 – 7/2	8 – 8
323.90	9.87×10^{-1}	94.10 – 30958.50	$3d^2(^3F)4s - 3d^2(^3F)4p$	$^4F - ^4F°$	5/2 – 5/2	6 – 6
324.20	1.16	0.00 – 30836.32	$3d^2(^3F)4s - 3d^2(^3F)4p$	$^4F - ^4F°$	3/2 – 3/2	4 – 4
325.19	3.38×10^{-1}	94.10 – 30836.32	$3d^2(^3F)4s - 3d^2(^3F)4p$	$^4F - ^4F°$	5/2 – 3/2	6 – 4
325.29	3.9×10^{-1}	225.73 – 30958.50	$3d^2(^3F)4s - 3d^2(^3F)4p$	$^4F - ^4F°$	7/2 – 5/2	8 – 6
325.42	2.0×10^{-1}	393.44 – 31113.65	$3d^2(^3F)4s - 3d^2(^3F)4p$	$^4F - ^4F°$	9/2 – 7/2	10 – 8
331.80	6.0×10^{-2}	983.89 – 31113.65	$3d^31 - 3d^2(^3F)4p$	$^4F - ^4F°$	5/2 – 7/2	6 – 8
333.52	2.93×10^{-1}	983.89 – 30958.50	$3d^3 - 3d^2(^3F)4p$	$^4F - ^4F°$	5/2 – 5/2	6 – 6
334.04	3.6×10^{-1}	908.02 – 30836.32	$3d^3 - 3d^2(^3F)4p$	$^4F - ^4F°$	3/2 – 3/2	4 – 4
336.12	1.1	225.73 – 29968.30	$3d^2(^3F)4s - 3d^2(^3F)4p$	$^4F - ^4G°$	7/2 – 9/2	8 – 10
337.28	1.11	94.10 – 29734.54	$3d^2(^3F)4s - 3d^2(^3F)4p$	$^4F - ^4G°$	5/2 – 7/2	6 – 8
338.03	1.6×10^{-1}	393.44 – 29968.30	$3d^2(^3F)4s - 3d^2(^3F)4p$	$^4F - ^4G°$	9/2 – 9/2	10 – 10
338.38	1.09	0.00 – 29544.37	$3d^2(^3F)4s - 3d^2(^3F)4p$	$^4F - ^4G°$	3/2 – 5/2	4 – 6
338.78	2.18×10^{-1}	225.73 – 29734.54	$3d^2(^3F)4s - 3d^2(^3F)4p$	$^4F - ^4G°$	7/2 – 7/2	8 – 8
339.46	2.5×10^{-1}	94.10 – 29544.37	$3d^2(^3F)4s - 3d^2(^3F)4p$	$^4F - ^4G°$	5/2 – 5/2	6 – 6
340.72	7.2×10^{-3}	393.44 – 29734.54	$3d^2(^3F)4s - 3d^2(^3F)4p$	$^4F - ^4G°$	9/2 – 7/2	10 – 8
340.98	1.2×10^{-2}	225.73 – 29544.37	$3d^2(^3F)4s - 3d^2(^3F)4p$	$^4F - ^4G°$	7/2 – 5/2	8 – 6
347.72	6.05×10^{-2}	983.89 – 29734.54	$3d^3 - 3d^2(^3F)4p$	$^4F - ^4G°$	5/2 – 7/2	6 – 8

$$\mathrm{Ti}(m) + e \Leftrightarrow \mathrm{Ti}(n) + h\nu$$
$$\mathrm{Ti}^{+}(m) + e \Leftrightarrow \mathrm{Ti}^{+}(n) + h\nu \quad (5)$$

The equations system, which describes the kinetics processes involving neutral atoms, ions and electrons, has the form:

$$\frac{\partial Na_m}{\partial t} = \sum_{n \lhd m} Ad(T_{ra})_{nm} \cdot Na_n + \sum_{l \lhd m} Ar(T_{ra})_{lm} \cdot Na_l - \sum_{n \rhd m} Ar(T_{ra})_{mn} \cdot Na_m - \sum_{l \lhd m} Ad(T_{ra})_{ml} \cdot Na_m - \sum_{l \lhd m} Kd(T_e)_{ml} \cdot Na_m \cdot N_e + \sum_{l \lhd m} Kr(T_e)_{ml} \cdot Na_l \cdot N_e + \sum_{n \rhd m} Kd(T_e)_{nm} \cdot Na_n \cdot N_e + \sum_{n \rhd m} Kr(T_e)_{mn} \cdot Na_m \cdot N_e - \sum_i Id(T_e)_{mi} \cdot Na_m \cdot N_e + \sum_i Rr(T_e)_{im} \cdot Ni_i \cdot N_e^2 - \sum_i Fd(T_{ra})_{mi} \cdot Na_m + \sum_i Fr(T_e, T_{ra})_{im} \cdot Ni_i \cdot N_e - V_{am} \quad (6)$$

$$\frac{\partial Ni_m}{\partial t} = \sum_{n \rhd m} Ad(T_{ri})_{nm} \cdot Ni_n + \sum_{l \lhd m} Ar(T_{ri})_{mn} \cdot Ni_l - \sum_{n \rhd m} Ar(T_{ri})_{mn} \cdot Ni_m - \sum_{l \lhd m} Ad(T_{ri})_{ml} \cdot Ni_m - \sum_{l \rhd m} Kd(T_e)_{ml} \cdot Ni_m \cdot N_e + \sum_{l \lhd m} Kr(T_e)_{ml} \cdot Ni_l \cdot N_e + \sum_{n \rhd m} Kd(T_e)_{nm} \cdot Na_n \cdot N_e + \sum_{n \rhd m} Kr(T_e)_{mn} \cdot Ni_m \cdot N_e - \sum_i Id(T_e)_{mi} \cdot Na_i \cdot N_e + \sum_m Rr(T_e)_{im} \cdot Ni_i \cdot N_e^2 - \sum_i Fd(T_{ra})_{mi} \cdot Na_i + \sum_i Fr(T_e, T_{ra})_{im} \cdot Ni_m \cdot N_e - V_{im} \quad (7)$$

$$\frac{\partial N_e}{\partial t} = \sum_{m,i} Id(T_e)_{mi} \cdot Na_m \cdot N_e - \sum_{i,m} Rr(T_e)_{im} \cdot Ni_i \cdot N_e^2 + \sum_{m,j} Fd(T_{ra})_{mi} \cdot Na_m - \sum_{i,m} Fr \times (T_e, T_{ra})_{im} \cdot Ni_i \cdot N_e - V_e \quad (8)$$

Here, Na_m and Ni_m are the titanium atom and ion population densities in the excited state m. The values of $Ad(X)_{nm}$, $Ad(X)_{ml}$, $Ar(X)_{mn}$, $Ar(X)_{lm}$ and $Kd(T_e)_{nm}$, $Kd(T_e)_{ml}$, $Kr(T_e)_{lm}$, $Kr(T_e)_{mn}$ denote the rate constants of radiation reabsorption, of emission processes (spontaneous and stimulated emission), of the inelastic and superelastic collisions of atoms and ions with electrons. As a result, the population density of state m is governed by forward and backward transitions of the particles to the upper levels l and from the lower levels n. The value of X is equal to T_{ra} for atoms and T_{ri} for ions, where T_{ra} and T_{ri} specify the effective temperatures of the local spectral densities of radiation for atoms and ions. $Id(T_e)_{mi}$, $Fd(X)_{mi}$ and $Rr(T_e)_{im}$, $Fr(X,T_e)_{im}$ are the rate constants of forward processes such as ionization by electron impact and photo-ionization, by radiation of the LIP and by ultra violet radiation of excimer laser of atoms, in the excited state m, of backward processes of three body recombination and of the radiative recombination of ions in the excited states i.

The rate constants of the processes were calculated on the basis of relationships taken from [31–36]. While the cross-sections of inelastic and superelastic collisions of atoms and ions with electrons, of ionization of the titanium atoms by electron impacts, of photo-ionization of atoms and of radiative recombination of ions are taken from [33–35].

The proposed computational model considers most of the spectral transitions for titanium atoms and ions with lower levels, which as we expect, are characterized by the high values of population density. These spectral lines can be strongly absorbed by atoms and ions. It is well known [32] that radiation of such spectral lines, which are

strongly absorbed, reach the partial local thermodynamic balance with atoms and ions in the electronically excited states. For this reason, it is reasonable to assume that temperatures T_{ra} and T_{ri}, corresponding to the local spectral densities of radiation for atoms and ions, are coincident with those of atoms T_a and ions T_i characterizing ASDF and ISDF.

One of the most important characteristics of the LIP is the electron energy distribution function (EEDF). For the test conditions specified above, we assume that the EEDF is Maxwell distribution function. The validity of this assumption is justified by the high ionization degree of the LIP [24]. Note that obtained values of the rate constants of the inelastic and superelastic collisions of ions with electrons considerably exceed, by more than two orders, those of atoms with electrons, in the range of the electron temperature from 10 000 to 30 000 K. Therefore, the relaxation time of excited states of ions, when the temperature of ions is equal to that of the electrons, is much shorter than the corresponding time for excited states of atoms. This suggests the reliability of the assumption that the temperature of ions is coincident with that of electrons.

The rate constants of stimulated emission and reabsorption for ion, electron − atom and electron − ion collisions are recalculated in the course of solving the equation system for population density as the electron temperature is changed. We might add that the calculations are performed for the measured time dependence of the ionic temperature, which, as above mentioned, may be assumed to coincide with that of the electron under the conditions of our experiment.

The values of V_{am}, V_{im} and V_e express the decrease of titanium atom and ion population densities and of electron number density due to the LIP expansion. In order to magnify the reliability of numerical simulation and, thus, to achieve the best agreement between calculated and measured data, we apply an approach involving a principle which inserts experimental data into the integrated kinetic equation system. In this approach, V_{am}, V_{im} and V_e are proportional to the population density of atoms and ions in the excited states and electron number density, respectively [18]. The coefficients of proportionality are time variable functions, which are approximated by the exponential decay functions describing the decrease of the spectral line intensities of ions and atoms observed in our experiment. The parameters of the coefficient in these expressions were chosen from the best conformity between results of numerical simulations and measurements of electron number density. As will be shown below, the approach is reasonable and avoids labor-intensive calculations connected with the LIP dynamics expansion.

The equation system is solved by the method described in detail in [37]. Actually, we consider the vaporization stage only in order to determine the initial conditions for the expansion stage. Therefore, at $t = 0$ ns, ASDF and ISDF corresponds to the Boltzmann distribution at a temperature of 10 000 K. This initial temperature is a typical surface temperature of a solid target during ultra violet laser irradiation [9] and so it was assumed that the species leave the surface in their equilibrium proportion, at the same temperature as the target surface [18]. According to this assumption we calculated, by means of the Saha–Boltzmann equation, the initial electron number density and the initial neutral number density as input data for the numerical simulations. For a strictly correct treatment of the physical phenomena, the initial temperature of Boltzmann distribution should take into account the temperature gradient that rises from the center towards the periphery of target materials heated by the incident laser radiation. Calculations, however, shows that these input data do not affect the evolution of ASDF and ISDF in the numerical model proposed in this work.

4. Results and discussion

4.1. Laser induced plasma emission

The emission spectra of the LIP, observed at 0.6 mm from the target surface, as a result of the interaction of laser radiation with TiO and TiO_2 target materials, differs very slightly. Fig. 2 illustrates typical fragments of time — integrated

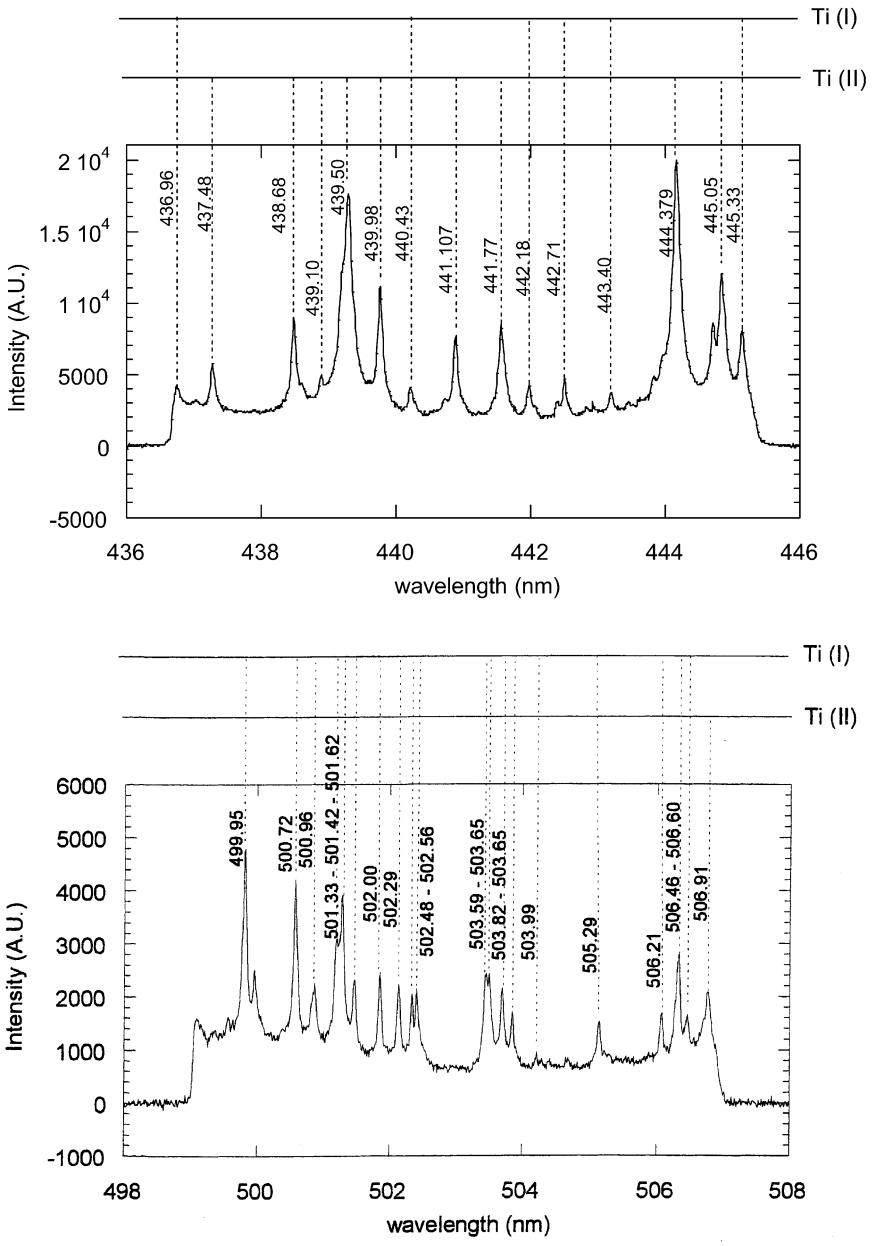

Fig. 2. Typical fragments of the emission spectrum of the TiO_2 plasma generated by KrF excimer laser ablation (a) in the spectral range of 436–446 nm and (b) 498–508 nm, at the following experimental conditions: laser fluence = 6 J cm^{-2}, distance from the target = 0.6 mm, oxygen pressure = 10^{-2} torr, gate width = 2 μs.

emission spectra of the KrF — laser-induced plasma. A number of characteristic titanium lines are observed and interpreted as emission from the excited neutral atoms and from single-charged ions (TiI and TiII). A higher degree of ionic spectral lines, such as TiIII and TiIV, were not clearly observed at the laser fluences employed in these experiments. The intricacy of the titanium spectrum, in the investigated spectral range (250–700 nm), is caused by the complexity of the

atomic and ionic titanium electronic configuration system [38].

In contrast, the intensity of the spectral lines corresponding to the transitions between the excited states of the oxygen atoms OI and ions OII are too low with respect to the intensity of the titanium lines or they are too overlapped by strong nearby lines to be clearly identified in the investigated spectral range. In addition, a feature of the TiO and TiO_2 spectra is that strong clear bands resulting from dissociation products of the TiO_2 (e.g. titanium TiO, oxygen O_2 and molecular oxygen ions) are not observed. Note that the obtained results regarding the spectral observations are consistent with the results reported in [12,39].

On the basis of emission spectra identification, by the use of tabulated atomic lines and molecular bands [29,30], for the analysis of the spectral distribution of line intensities and for the determination of ASDF and ISDF time evolution, six lines of titanium atoms and five lines of titanium ions, arising at the following transitions: 398.98, 464.5, 462.3, 461.7, 517.37, 519.29 and 288.49, 293.11, 293.59, 293.85 and 294.53 nm were chosen. These spectral lines were chosen because they are free from overlapping with neighboring lines and have emission times shorter or at least comparable with the time of residence of the LIP in the probe volume.

4.2. Spectral line intensity and broadening.

In order to minimize error in the determination of the area of spectral lines and, thus, to avoid the strong initial background continuum contribution to investigated spectral lines, we began our detection with an initial delay of 100 ns, at a distance of 0.6 mm from the target. This means that the spectroscopic monitoring starts some tenths of nanosecond after the front expansion of the LIP plume has passed the observation point. Fig. 3 shows typical temporal and spatial resolved emission spectra measurements, in the wavelength range from 398 to 404 nm, in various moments of time, 100, 140, 180, 260 and 300 ns from the laser pulse. In the time interval 100–180 ns, in Fig. 3, the residual continuous spectrum is also visible, caused by collisions of free electrons with heavy particles (ions and atoms) and the radiative recombination of the electrons with

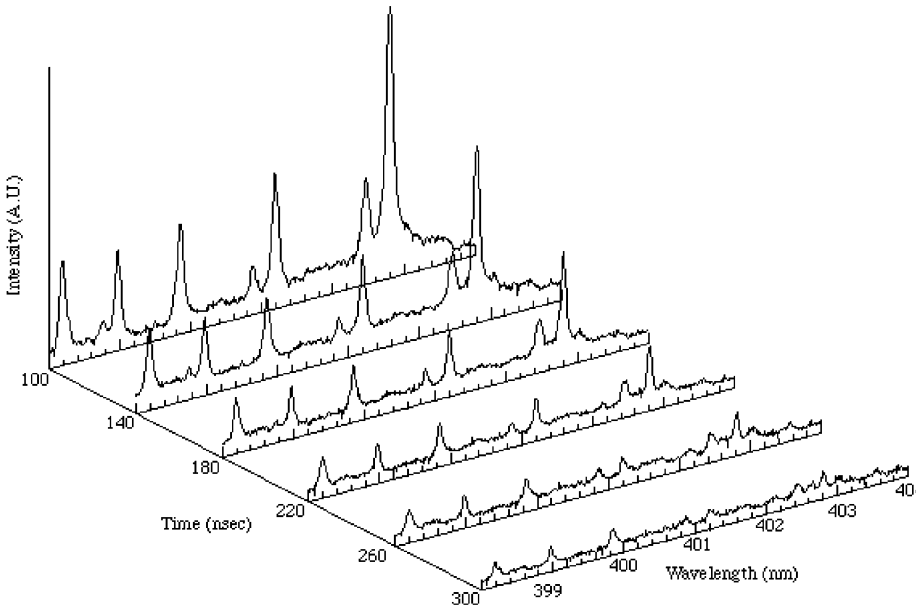

Fig. 3. Evolution of the emission spectra of TiO plasma in vacuum for various delays: 100; 140; 180; 220; 260 and 300 ns. Gate width = 15 ns, laser fluence = 6 J cm^{-2}.

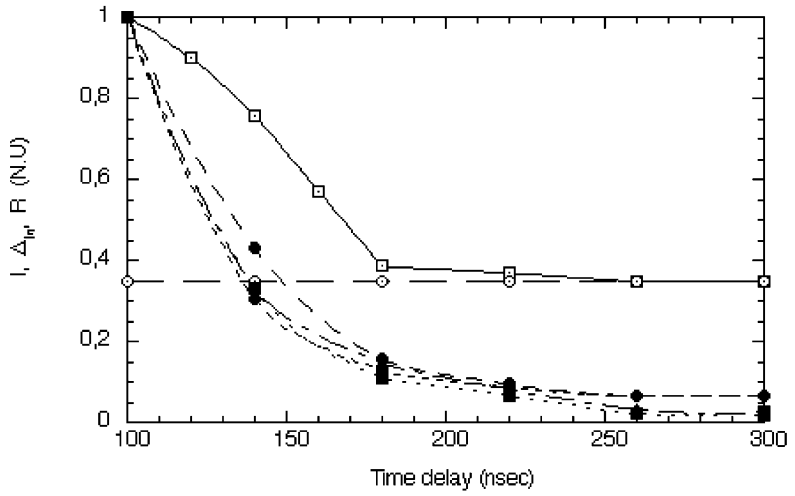

Fig. 4. Normalized time evolution of the Voigt profile parameter R (□), instrument function Δ_{in} (○) and ionic spectral line intensities I, at 288.49 (▼), 293.11 (●), 293.59 (■) and 294.53 nm (▲) in vacuum. Gate width = 15 ns, laser fluence = 6 J cm^{-2}, distance from target = 0.6 mm.

positive ions. This implies that the LIP generation has been finished, at a gate delay of 100 ns, and the influence of the continuum emission on the titanium spectral lines can be neglected. As can be observed from Fig. 3, the signal rapidly declines for two reasons: firstly, at this experimental condition, the LIP dynamics can be compared to free expansion in vacuum [19] and secondly, as reported in [40] the LIP produced by UV laser has shorter times.

A typical time evolution of the normalized Voigt profile parameter R, corresponding to the atomic spectral line at 462.3 nm, the instrument function width Δ_{in} and the ionic spectral line intensities are presented in Fig. 4. The appreciable reduction of the ionic line intensities are decreased mainly because of the LIP expansion during which different kinetic processes succeed, as already discussed above. This is accompanied by an abrupt diminution of linewidths of the lines from their maximum values, 1.5–0.9 A, which coincides with the width of the instrument function at the time of 180–200 ns.

The parameter R defines the typology of the line shape and is equal to the ratio of the Lorenzian and Gaussian widths of the spectral line. The measured spectral line shape of the atomic and ionic lines are approximately Lorenzians at the stage of the LIP time evolution from 100 to 180 ns. It is reasonable to suggest that, for our experimental conditions, the main mechanism of atomic and ionic spectral line broadening is the quadratic Stark effect. This is confirmed by the experimental interrelation between the time evolution of the ionic spectral line intensities and spectral line widths. As can be drawn from Fig. 4, the parameters R is appreciably decreased. This means that the spectral line shape is transformed from Lorenzian shape to the instrument function shape, which is accompanied by the drastic decreasing of its linewidth and the ionic spectral line intensities. Thus, it is possible to conclude that, the dominant mechanism of line broadening of heavy particles is mainly due to collisions of the electrons with atoms and ions.

All data for the estimation of the electron number density on selected spectral lines were taken from other studies [41–43]. For the definition of the electron number density it is necessary to know the values of the electron temperature. We used experimental values of electron temperature measured in the present work, which are presented below. The temporal evolution of the electron number density determined from the quadratic Stark-broadening of the spectral lines is presented in Fig. 5 as a function of the gate delay

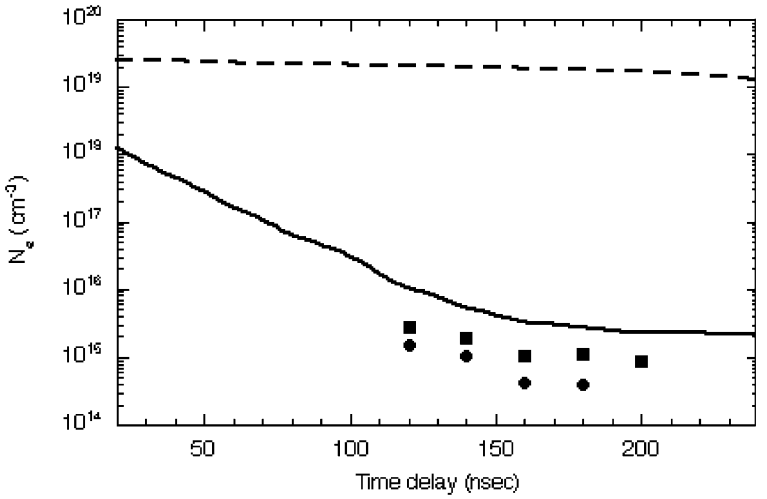

Fig. 5. Temporal evolution of electron number density obtained by quadratic Stark broadening of spectral lines at the laser fluence of 6 J cm^{-2} (■) and 1.75 J cm^{-2} (●). It also showed the electron number density recovered by the numerical modeling with and without considering the LIP expansion, solid and dashed curves, respectively.

from 100 to 180 ns. The points indicate experimental results at the different values of the laser fluence. The measured electron number density is weakly decreased from 3.5×10^{15} to 1×10^{15} cm^{-3} at the laser fluence of 6 J cm^{-2}. Fig. 5 demonstrates that the electron number density increases from 10^{14} to 10^{15} cm^{-3} with an increase in the laser fluence from 1.75 to 6 J cm^{-2}. It is also showed that the electron number density, recovered by the numerical modeling with and without considering the LIP expansion, respectively, produced solid and dashed curves. A comparison of experimental results with results of the numerical modeling follows, time evolution of the electron number density is mainly caused by the high speed of the LIP expansion, in an interval of the gate delay from 30 to 180 ns. The consecutive involvement of channels for neutralization and the occurrence of charged particles such as ionization of atoms by electron impact, three body recombination, photo-ionization and photo-recombination do not markedly influence the results of calculation of electron number density dynamics. The slow change of electron number density after 180 ns is obtained because of the reduced expansion rate. In this stage, the rate constant of three body and radiative recombinations is no longer affected by the rapid change in species concentration due to the LIP expansion.

4.3. Atomic and an ionic state distribution functions

The ASDF and ISDF were recovered from the experimental spectrum measured at different values of laser fluence, of distance from the targets, of the oxygen pressure, at 10^{-2}–10^{-1} torr and in vacuum.

Fig. 6 shows a comparison of the typically measured (a) and calculated (b) ASDF, at a distance of 0.6 mm from the target surface, at 260 ns from the beginning of the laser radiation interaction with the target in vacuum. The circular points with error bars (see Fig. 6a) indicate the experimental relationship between $\ln(N_m/g_m)$ and the energy of the atomic excited states. Here, N_m is the population density of the excited state m. The diamond points (see Fig. 6b) are a result of the numerical simulation of the population density dependence on the energy of the excited states. Note that Fig. 6b also presents values of $\ln(N_m/g_m)$ corresponding to the ground state and a set of metastable states of the titanium atoms and thus, it demonstrates that the ASDF experimental pattern holds for all the electronic states

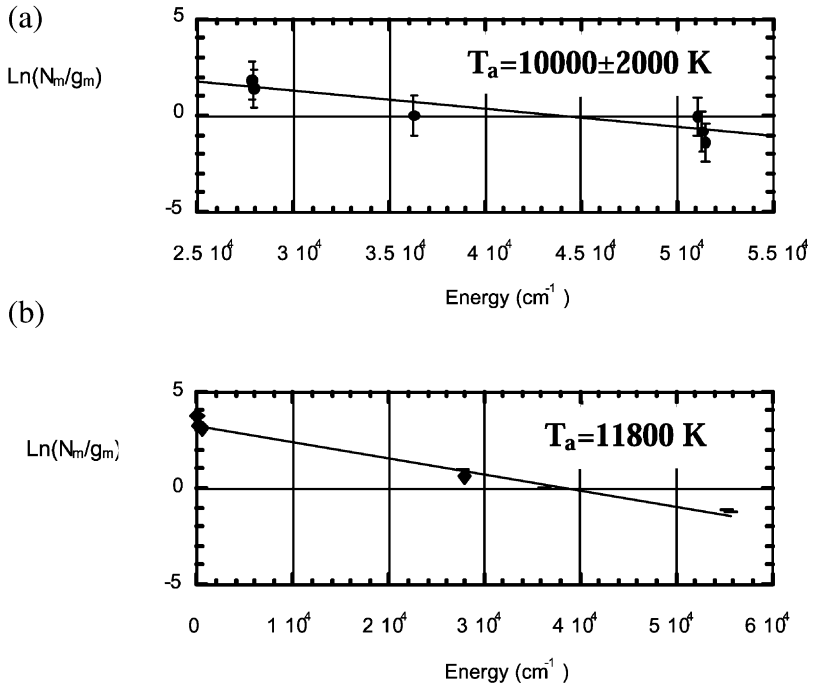

Fig. 6. Measured (a) and calculated (b) ASDF at 260 ns from the laser pulse at the laser fluence of 6 J cm^{-2} and 0.6 mm from the TiO target in vacuum.

considered in this model. An analogous result was obtained for ISDF.

Using Boltzmann's plot technique (solid lines) we have determined the temperatures of atoms and ions by the relative atomic and ionic line intensity measurements and by the values of $\ln(N_m/g_m)$ predicted by the model. As was observed, after the laser pulse, for 300 ns, the experimental and the calculated population densities of atoms and ions can be represented, in good approximation, in a Boltzmann form. Fig. 6a,b shows that the temperatures obtained experimentally, $10\,000 \pm 2000$ K and by simulation, 11 800 K, are in good agreement over a wide range of the gate delay (100–300 ns). Thus, it is assumable that for an adequate description of time evalution of atom and ion population density in the LIP, it is reasonable to insert the concept of temperature, for atoms T_a and for ions T_i corresponding to each, measured using a distribution function [31].

Fig. 7 shows a typical plot of the time evolution of the values of ion and atom temperatures derived by the measured ASDF and ISDF, during the LIP expansion in vacuum from 100 to 300 ns at distance of 0.6 mm from the targets surface represented by solid and dashed curves and the results of the ion and atom temperatures obtained by numerical simulation, which are in good agreement with the experimental results. As can be seen from Fig. 7, the temperatures of ions and atoms are appreciably different. Variation of atom temperature is insignificant in time and it changes from 11 000 to 8000 K, whereas ion temperature markedly decreased from 30 000 to 12 000 K.

According to the analysis of the equation system solutions for population density, the timescale of the LIP evolution can be divided into two stages: an early stage, corresponding to the time interval up to 10 ns from beginning of the laser pulse; and a later stage from 10 to 300 ns. The experimental discrepancy in temperature of ions

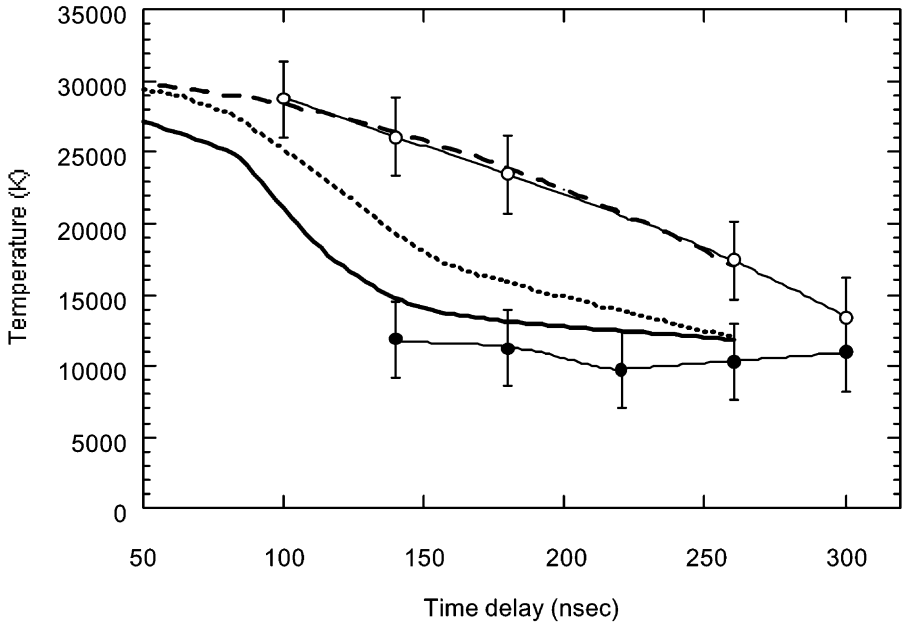

Fig. 7. The late stage of temporal evolution of the atomic and ionic temperatures: experimental values for atoms (●) and ions (○) are compared to results of numerical modeling, represented by solid and dashed curves at a laser fluence of 6 J cm^{-2}, at a distance of 0.6 mm from the TiO target in vacuum. It is also presented by a dotted curve, the numerical model result for ions, without considering the stimulated emission and reabsorption mechanisms.

and atoms arises as a consequence of the deviation from the LTE conditions at a later stage of temporal evolution of the LIP.

In the early stage we suppose that the LIP fulfills LTE conditions. Fig. 8 shows the time evolution of the electron number density, of atom and ion temperatures calculated by the numerical model proposed. It demonstrates that the elec-

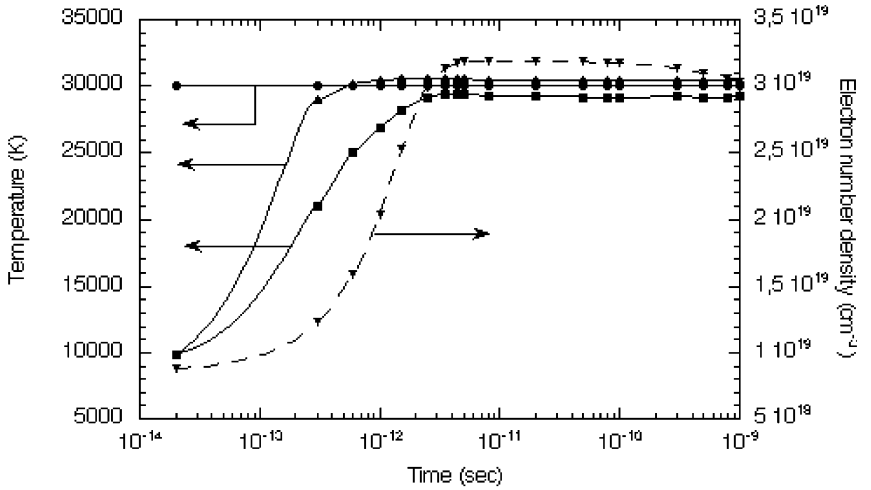

Fig. 8. The early stages of temporal evolution of electron number density (▼), electron temperature (●), atomic (■) and ionic (▲) temperatures estimated by numerical modeling.

tron number density and the atom and ion temperatures quickly reach the LTE conditions in a nanosecond, which is in agreement with [18] where a model for UV LIP in vacuum condition is reported. After this time ASDF and ISDF strictly obey the Boltzmann relationship and heavy particles and electrons reach the same temperature. The presence of the Boltzmann relationship at the same electron temperature testifies that the initial stage of the LIP evolution time is caused mainly by excitation and de-excitation processes of the electronic excited states of atoms and ions by electron impacts. The numerical simulation demonstrates that, within the framework of the proposed model in the time interval up to 5–10 ns, the effect of radiative and reabsorption processes on the population density of electronically-excited states of titanium atoms and ions can be neglected. The population density is also changed as a result of the processes of the ionizations and of the recombinations and, as the calculations indicate, the role of these processes is paramount for an establishment of partial equilibrium between excited heavy particles (atoms and ions) and electrons. The calculated values of the electron number density vary from 10^{18} to 10^{20} cm^{-3} and coincide with those recovered from the Saha equation at electron temperatures from 25 000 to 30 000 K. Thus, it is reasonable to suggest the existence of the LTE conditions, which take place near the target, during the 5–10 ns after laser pulse, at the laser fluence from 1.7 to 6 J cm^{-2}.

As discussed above, the time dependence of the electron number density and of the population density of atoms and ions, corresponding to the late stage of the LIP time evolution, are mainly caused by gas dynamic expansion of the plasma. At the initial stage of the plasma expansion from 30 to 180 ns, the electron number density dramatically decreases from values obtained under LTE conditions to those determined by the quadratic Stark-broadening of the atomic spectral lines. By the analysis of the equation system solutions it follows that the explanation of the observable discrepancy of atom and ion temperatures lies in the electron number density decreasing and therefore, in the change of the kinetic mechanism hierarchy determining the late stage dynamics of ASDF and ISDF.

In the late stage, mainly the electron impact excitation and de-excitation of the atom population density and the decay of the excited states of atoms by spontaneous emission governed ASDF time evolution. This is clearly demonstrated in Fig. 9, where a comparison of ASDF numerical simulation results with considered channels of decay, by spontaneous emission of the excited states of atoms and without this process, are presented. It shows that, at the measured electron

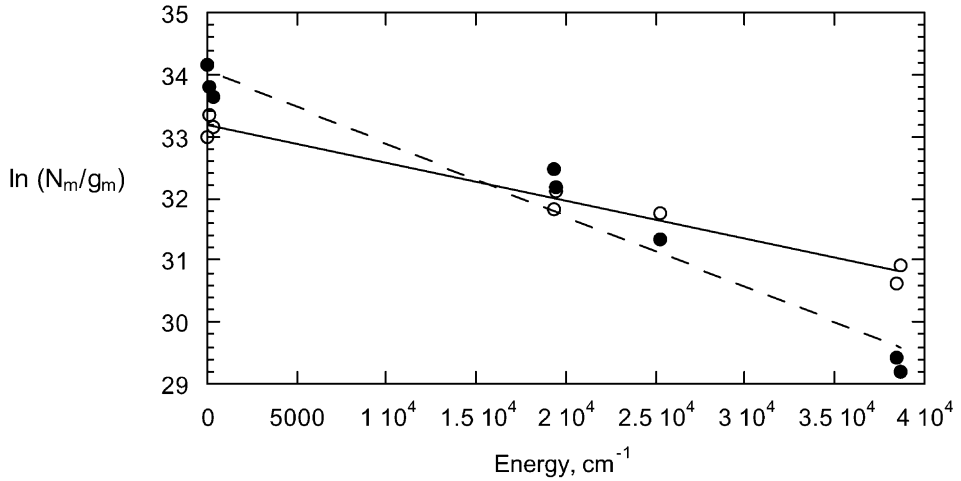

Fig. 9. Numerical simulation results of ASDF without (○) and with (●) considering the spontaneous emission mechanism.

number density $\approx 10^{14}$–10^{15} cm^{-3}, the population density of the excited states are underpopulated, whereas the population density of the ground state is overpopulated in comparison with their values at the LTE conditions and at the same electron temperature. This implies the decompensation of atoms excitation reactions and the violation of the detailed balance principle are caused by radiative processes such as spontaneous emission, reabsorption and stimulated emission. As this takes place, it is significant that the electron temperature is different from the temperature of atoms corresponding to the calculated ASDF. The same phenomena for ASDF is observed in our experiments. The quantitative agreement of calculations with experiments for ASDF, presented on Fig. 7, argues in favor of the interpretation that change in the population density of atoms occurs more efficiently as a result of the inelastic and superelastic collisions of electrons with atoms in electronically-excited states and decay by spontaneous emission. Thus, a really important assumption, such as an optically thin plasma, is applicable for these experimental conditions. However, the temperatures deduced from the calculated and measured ASDF and the electron temperature strongly differed, owing to violation of the LTE conditions in the LIP.

However, the reabsorption and stimulated emission reactions, alongside processes of inelastic and superelastic collisions of electrons with ions in the electronically-excited states and decay by spontaneous emission, play an important role in the kinetics of the ISDF time evolution. The process of radiation reabsorption by ions in the ground state destroys the cause of the deviation of the ion population density from those under LTE conditions, as depicted in Fig. 7. A comparison of the results of the numerical simulation of ISDF with (dashed line) and without (dotted line) these processes demonstrates that including the reabsorption contribution, it results in the coincidence of the electron temperature with that of the ions. The fundamental meaning of this consideration allows the electron temperature to be determined from measurements of ISDF. However, it is essential to take into account the fact that the spectral characteristics of resonance lines of ions are affected by a greater degree of reabsorption with respect to the atomic lines. For this reason, we used spectral lines of atoms for the determination of electron number density and ion temperature was defined from relative non-resonance ionic line intensity measurements.

Referring to Fig. 10, the ion temperature increases from 25 000–11 000 to 31 000–14 000 K with an increase in the laser fluence from 1.75 to 6 J cm^{-2}, whereas the growth of the atom temperature is insignificant. In our experiments, we observed that the atomic and ionic temperatures slightly depended on the background oxygen pressure. As illustrated Fig. 10, with an increase in the oxygen pressure up to 10^{-1} torr, the atomic temperature tends to decrease slightly close to the target (0.6 mm). The kinetic mechanisms, as discussed above, triggering ASDF and ISDF temporal evolution retaining their validity for long distances from the target, up to 6 mm as demonstrated by the observed experimental discreapancy of the ionic and atomic temperatures in Fig. 11. Note that measurements as function of distance were performed by a wide gate (2 μs), using an external pulsed generator as main trigger for the KrF laser and for the detector system in order to detect whole the LIP spectral signal.

5. Conclusions

To summarize, the present study was devoted to the experimental and theoretical investigation of electron number density and temperature, ASDF and ISDF time evolution of the LIP at a laser fluence of 1.75–6 J cm^{-2}, distance of 0.6 mm from the TiO and TiO_2 targets, oxygen pressure of 10^{-2}–10^{-1} torr and in vacuum. A state-to-state collisional radiative model describing kinetic processes, taking place at a distance of 0.6 mm from the target surface, for a delay time of LIP monitoring from 100 to 300 ns from the laser pulse, was, for the first time, proposed to determine the time duration of the LTE in expanding plasma and to interpret the observed discrepancy of ion, electron and atom temperatures in our experiments.

According to the kinetic model, the LTE condi-

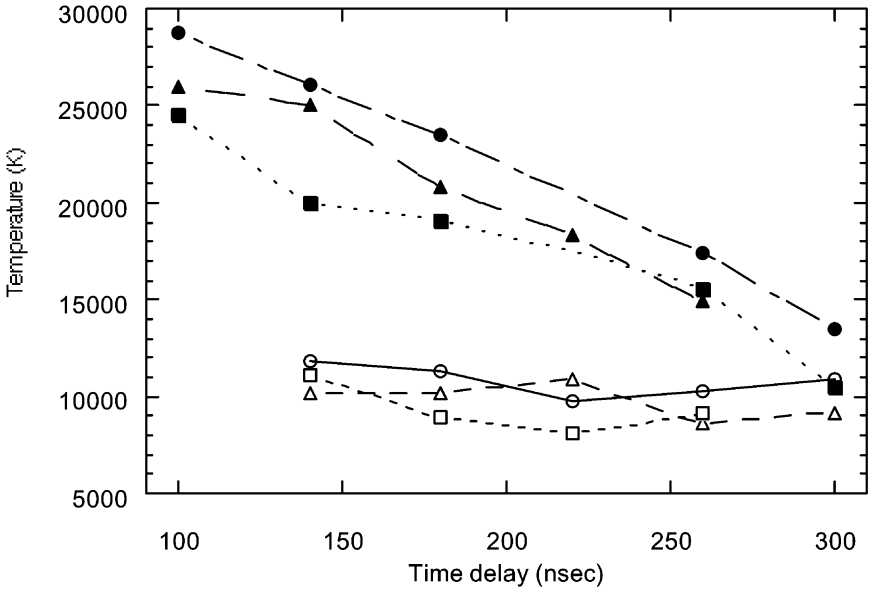

Fig. 10. Experimental temperatures of atoms and ions at different experimental conditions: for atoms (○) laser fluence = 6 J cm^{-2} in vacuum, (△) laser fluence = 6 J cm^{-2}, oxygen pressure = 10^{-1} torr, (□) laser fluence = 1.75 J cm^{-2}. For ions (●) laser fluence = 6 J cm^{-2} in vacuum, (▲) laser fluence = 6 J cm^{-2}, oxygen pressure = 10^{-1} torr, (■) laser fluence = 3 J cm^{-2}.

tions, which take place at a distance of 0.6 mm from targets, occur during the 5–10 ns after laser pulse. After this time, a comparison of the experimental and calculated results reveals that the non-equilibrium effect is related to the deviation from the detailed principle balance, caused by radiative processes such as spontaneous emission, reabsorption and stimulated emission, as a consequence of the electron number density decrease, due to the LIP expansion during 30–180 ns. Under our experimental conditions, ASDF time evolution is mainly governed by excitation and de-excitation of the electronically excited states of atoms by electron impacts and decay by spontaneous emission, which causes deviation of the electron and ion temperature from that of the atoms. However, processes of reabsorption and stimulated emission, along with the above-mentioned processes, play an important role in the kinetics of ISDF time evolution and destroy the

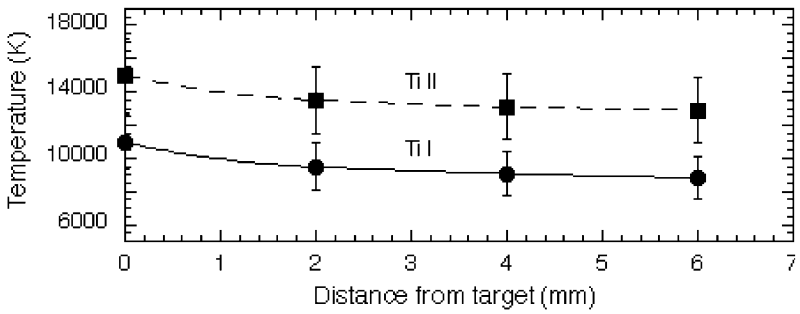

Fig. 11. Experimental values of ionic and atomic temperatures as a function of the distance from the target. Laser fluence = 1.5 J cm^{-2}; oxygen pressure = 10^{-2} torr, distance from TiO_2 target = 0.6 mm, gate width = 2 μs.

cause of deviation from LTE conditions. In this respect, the electron number density was determined from the atomic spectral line shapes analysis. At the same time, electron temperatures were recovered from non-resonance ionic spectral line intensity measurements by Boltzmann's plot technique.

Acknowledgements

This work was supported by CNR/P.F. Materiali Speciali per Tecnologie Avanzate (contract #97.01005.34). The authors are grateful to Prof. M. Capitelli, Dr M. Snels and Dr G. Friel for showing interest in this study and for taking part in our discussion.

References

[1] D.B. Chrisey, G.K. Huber, Pulsed Laser Deposition of Thin Films A, Wiley-Interscience Publication, New York, 1994.
[2] M. Ohring, Materials Science of Thin Films, Academic Press, Boston, 1997.
[3] Y.A. Bykovskii, V.M. Boyakov, V.T. Galochkin, A.S. Molchanov, I.N. Nikolaev, A.N. Oraevskii, Deposition of metal, semiconductor, and oxide films with a periodically pulsed CO_2 laser, Sov. Phys. Tech. 23 (5) (1978) 578–581.
[4] A.G. Akimov, A.P. Gagarin, V.G. Dagunov, V.S. Makin, S.D. Pudov, Composition of an oxide film formed after pulsed heating of a metal, Sov. Phys. Tech. 25 (11) (1980) 1439–1441.
[5] C.M. Dai, C.S. Su, D.S. Chuu, Composition and chemical reactions of titanium oxide films deposited by laser evaporation, J. Appl. Phys. 69 (6) (1991) 3766–3768.
[6] H.O. Sankur, W. Cunning, Deposition of optical thin films by pulsed laser assisted evaporation, Appl. Optics 28 (14) (1989) 2806–2808.
[7] V.A. Shakhatov, A. De Giacomo, V. D'Onghia, Plasma assisted pulsed laser deposition of titanium dioxide in: V.I. Pustolov, V. Komunov (Eds.), ALT 99 International Conference: Advanced Laser Technologies: Proceedings of SPIE 4070, SPIE, 1999, p. 394.
[8] P.R. Willmott, J.R. Huber, Pulsed laser vaporization and deposition, Rev. Modern Phys. 72 (1) (2000) 315–328.
[9] S.S. Chu, M. Ye, C.P. Grigoropoulos, Spectroscopic Characterization of Laser-Induced Titanium Plume, Proccedings 5th ASME/JSME, ASME/JSME, San Diego, California, USA, March 15–19, 1999, pp. 1–5.
[10] X.T. Wang, B.Y. Man, G.T. Wang, Z. Zhao, B.Z. Xu, Y.Y. Xia, L.M. Mei, X.Y. Hu, Optical spectroscopy of plasma produced by laser ablation of Ti alloy in air, J. Appl. Phys. 80 (3) (1996) 1783–1786.
[11] B.Y. Man, Particle velocity, electron temperature, and density profiles of pulsed laser-induced plasmas in air at different ambient pressures, Appl. Phys. B 67 (1998) 241–245.
[12] M.H. Hong, Y.F. Lu, T.M. Ho, L.W. Lu, T.S. Low, Plasma diagnostics in KrF excimer laser deposition of Ti thin films in: D. Shu-Sun, S.L. Wang (Eds.), Laser Processing of Materials and Industrial Application II: Proccedings of SPIE 3550, SPIE, 1998, p. 441.
[13] F. Fuso, L.N. Vyacheslavov, G. Masciarelli, E. Arimondo, Stark broadening diagnostics of the electron density in the laser ablation plume of $Yba_2Cu_3O_{7-x}$ and $PbZr_xTi_{x-1}O_3$, J. Appl. Phys. 76 (12) (1994) 8088–8096.
[14] O.A. Bukin, I.V. Bazarov, N.S. Bodin, A.A. Il'in, V.D. Kiselev, E.A. Sviridenkov, V.I. Tsarev, A.Yu Major, Influence of the pressure of a gaseous, atmosphere on the characteristics of the emission spectra of a laser plasma generated on the surfaces of solid targets, Quantum Electron. 28 (8) (1998) 685–688.
[15] S. Yalcin, D.R. Crosley, G.P. Smith, G.W. Faris, Influence of ambient conditions on the laser air spark, Appl. Phys. B 68 (1999) 121–130.
[16] H.R. Griem, Plasma Spectroscopy, McGraw-Hill Book Company, New York, 1964.
[17] R.H. Huddlestone, S.L. Leonard, Plasma Diagnostic Techniques, Academic Press, New York — London, 1965.
[18] S. Amoruso, Modeling of UV pulsed-laser ablation of metallic targets, Appl. Phys. A 69 (1999) 323–332.
[19] G. Colonna, A. Casavola, M. Capitelli, On the modeling of TiO plume expansion under laser ablation in: V.I. Pustolov, V. Komunov (Eds.), ALT 99 International Conference: Advanced Laser Technologies: Proceedings of SPIE 4070, SPIE, 1999, p. 293.
[20] R.K. Singh, J. Narayan, Pulsed-laser evaporation technique for deposition of thin films, Phys. Rev. B 41 13 (1990) 8843–8859.
[21] H.M. Urbassek, J. Mitchel, A gas flow model for the sputtering of condensed gases, Nucl. Instrum. Methods Phys. Res. B 22 (1987) 480–490.
[22] R. Kelly, R.W. Dreyfus, Primary and secondary mechanism in laser sputtering, Nucl. Instrum. Methods Phys. Res. B 65 (1992) 187–199.
[23] A.V. Bulgakov, N.M. Bulgakova, Dynamics of laser — induced plume expansion into an ambient gas during film deposition, J. Phys. D: Appl. Phys. 28 (1995) 1710–1718.
[24] M. Capitelli, F. Capitelli, A. Eletskii, Non-equilibrium and equilibrium problems in laser-induced plasmas, Spectrochim. Acta Part B 55 (2000) 559–574.

[25] J. Hermann, C. Boulmer-Leborgne, D. Hong, Diagnostics of the early phase of an ultraviolet laser induced plasma spectral line analysis considering self-absorption, J. Appl. Phys. 83 (2) (1998) 691–696.
[26] D. Ritter, J.C. Weisshaar, Kinetics of neutral transition-metal atoms in the gas phase: oxidation of Ti(a^3F) by NO, O_2 and N_2O, J. Phys. Chem. 93 (1989) 1576–1581.
[27] D. Ritter, J.C. Weisshaar, Kinetics of neutral transition-metal atoms in the gas phase: oxidation of Sc(a^2D), Ti(a^3F) and V(a^4F) by NO, O_2 and N_2O, J. Phys. Chem. 94 (1990) 4907–4913.
[28] D. Ritter, J.C. Weisshaar, Kinetics of excited-state Ti(a^5F) depletion by NO, O_2, N_2O and N_2, J. Phys. Chem. 97 (1993) 11480–11488.
[29] NIST Standard Reference Database 38: NIST Spectroscopic Properties of Atomic Ions Database (1992).
[30] C.E. Moore, United States Department of Commerce, National Bureau of Standards, Atomic Energy Levels, vol. I–III, 1949. Circular.
[31] L.M. Biberman, V.S. Vorobev, I.T. Yakubov, Kinetics of Non-Equilibrium Low Temperatures Plasmas, Consultants Bureau, New York and London, 1987.
[32] Y.P. Raizer, Physics of Gas Discharge, Nauka, Moscow, 1987 (in Russian).
[33] L.A. Vainshtein, I.I. Sobel'man, E.A. Yukov, Atoms Excitation and Spectral line broadening, Nauka, Moscow, 1979 (in Russian).
[34] L.A. Vainshtein, V.P. Shevel'ko, Ion structure and characteristics in the hot plasma, Nauka, Moscow, 1979 (in Russian).
[35] G.G. Chornyi, S.A. Losev, Physical — Chemical Processes in the Gas Dynamics, Computer Catalogue in three volumes. Volume I: Physical – Chemical Processes Dynamics in the Gas and Plasma, Moscow University, Moscow, 1995 (in Russian).
[36] V.G. Novikov, A.D. Solomaynnay, Plasma spectral characteristics correlated radiation', Teplofiz. Vysok. Temperat. 36 (6) (1998) 858–864 (in Russian)
[37] L.S. Polak, M.Y. Gol'denberg, A.A. Levitskii, Computational Methods in Chemical Kinetics, Nauka, Moscow, 1984 (in Russian).
[38] M.A. El'yashevich, Atomic and Molecular Spectroscopy, Fizmat, Moscow, 1962 (in Russian).
[39] H.F. Cheng, In situ spectroscopic examination of plasma emission during excimer laser deposition of $Pb_{0,58}La_{0,05}(Zr_{0,7}Ti_{0,3})_{0,9875}O_3$ thin films, Jpn. J. Appl. Phys. 34 (10) (1995) 5751–5757.
[40] A. Ciucci, V. Palleschi, S. Rastelli, R. Barbini, F. Colao, R. Fantoni, A. Palucci, S. Ribezzo, H.J.L. van der Steen, Trace pollutants analysis in soil by a time-resolved laser-induced breakdown spectroscopy technique, Appl. Phys. B 63 (1996) 185–190.
[41] H.J. Kusch, G. Meinhold, Druckverbreiterung von Titanlinien durch neutrale Argonatome, Zeitschrift für Astrophysik 66 (1967) 364–378 (in German).
[42] J. Meyer, Druckverbreiterung von Titanlinien durch neutrale Wasserestoffatome und Elektronen, Zeitschrift für Astrophysik 60 (1964) 94–105 (in German).
[43] M. Dahmen, H.J. Kusch, Druckverbreiterung und verschiebung von Titanlinien durch Argon', Zeitschrift für Astrophysik 68 (1968) 445–460 (in German).